Mon. Not. R. Astron. Soc. **000**, 000–000 (0000) Printed 10 July 2014 (MN LATEX style file v2.2)

On the use of semi-numerical simulations in predicting the 21-cm signal from the epoch of reionization

Suman Majumdar[1⋆], Garrelt Mellema[1]†, Kanan K. Datta[2], Hannes Jensen[1], T. Roy Choudhury[2], Somnath Bharadwaj[3] and Martina M. Friedrich[4]
[1]*Department of Astronomy & Oskar Klein Centre, AlbaNova, Stockholm University, SE-106 91 Stockholm, Sweden*
[2]*National Centre for Radio Astrophysics, Tata Institute of Fundamental Research, Pune - 411007, India*
[3]*Department of Physics and Centre for Theoretical Studies, Indian Institute of Technology, Kharagpur - 721302, India*
[4]*Centro de Ciencias de la Atmósfera, Universidad Nacional Autónoma de México, México*

arXiv:1403.0941v2 [astro-ph.CO] 9 Jul 2014

Accepted 2014 June 29. Received 2014 June 20; in original form 2014 March 4

ABSTRACT

We present a detailed comparison of three different simulations of the epoch of reionization (EoR). The radiative transfer simulation (C^2-RAY) among them is our benchmark. Radiative transfer codes can produce realistic results, but are computationally expensive. We compare it with two semi-numerical techniques: one using the same halos as C^2-RAY as its sources (Sem-Num), and one using a conditional Press-Schechter scheme (CPS+GS). These are vastly more computationally efficient than C^2-RAY, but use more simplistic physical assumptions. We evaluate these simulations in terms of their ability to reproduce the history and morphology of reionization. We find that both Sem-Num and CPS+GS can produce an ionization history and morphology that is very close to C^2-RAY, with Sem-Num performing slightly better compared to CPS+GS.

We also study different redshift space observables of the 21-cm signal from EoR: the variance, power spectrum and its various angular multipole moments. We find that both semi-numerical models perform reasonably well in predicting these observables at length scales relevant for present and future experiments. However, Sem-Num performs slightly better than CPS+GS in producing the reionization history, which is necessary for interpreting the future observations. The CPS+GS scheme, however, has the advantage that it is not restricted by the mass resolution of the dark matter density field.

Key words: methods: numerical – methods: statistical – cosmology: theory – dark ages, reionization, first stars – diffuse radiation

1 INTRODUCTION

The period in the history of the Universe during which the first sources of light were formed and the ionizing radiation from these objects gradually changed the state of hydrogen in the inter-galactic medium (IGM) from neutral (H I) to ionized (H II), is known as the epoch of reionization (EoR). Our knowledge regarding this epoch is currently very limited. Observations of the cosmic microwave background (CMBR) (Komatsu et al., 2011; Planck Collaboration et al., 2013) and absorption spectra of high redshift quasars (Becker et al., 2001; Fan et al., 2003; White et al., 2003; Goto et al., 2011) suggest that this era probably extended over the redshift range $6 \leq z \leq 15$ (Alvarez et al., 2006; Mitra et al., 2012). However, these observations are limited in their ability to shed light on many unresolved but important issues regarding the EoR, such as the precise duration and timing of reionization, the relative contributions from various kinds of sources, the properties of the major sources of ionization, the typical size and distribution of the ionized regions, etc.

Observations of the redshifted 21-cm signal from neutral hydrogen hold the possibility to address many of these issues. The brightness temperature of the redshifted 21-cm radiation is proportional to the H I density and is thus in principle capable of probing the H I distribution at the epoch where the radiation originated. This provides a unique possibility for tracking the entire reionization history. Motivated by this fact several low frequency radio interferometers such as GMRT[1] (Paciga et al., 2013), LOFAR[2] (Yatawatta et al., 2013; van Haarlem et al., 2013), MWA[3] (Tingay et al., 2013;

⋆ E-mail: smaju@astro.su.se
† E-mail: garrelt@astro.su.se

[1] http://www.gmrt.ncra.tifr.res.in
[2] http://www.lofar.org/
[3] http://www.haystack.mit.edu/ast/arrays/mwa/

Bowman et al., 2013), PAPER[4] (Parsons et al., 2013) and 21CMA[5] have already started devoting a significant amount of their observation time towards the detection of this signal. The future SKA[6] (Mellema et al., 2013) also has the detection of EoR 21-cm signal as one of its major scientific goals. However, our lack of knowledge about the properties of the ionizing sources and different physical processes involved during this era makes the forecast and interpretation of the expected signal and the interpretation of the observations of the redshifted 21-cm radiation very challenging.

A considerable amount of effort has already been devoted to simulate the expected EoR 21-cm signal. However, the major challenge in such modelling is the large number of unknown parameters involved and the huge dynamic range in terms of length scale and mass that one has to take into account. An accurate model of the EoR should in principle be able to follow the evolution of the dark matter, gas, radiation and ionizing sources along with various kinds of possible feedback processes involved. These simulations need to resolve the low-mass sources (dark matter halos of mass $\sim 10^8 - 10^9\ \mathrm{M}_\odot$) that are expected to dominate the reionization process. At the same time, simulation boxes need to be large enough ($\sim$ Gpc) to statistically sample the H I distribution at cosmological length scales and also to mimic the ongoing and future H I survey volumes. Numerical radiative transfer simulations which use ray-tracing to follow the propagation of ionization fronts in the IGM are capable of incorporating the detailed physical processes that are active during reionization (Gnedin, 2000; Ciardi et al., 2001; Ricotti et al., 2002; Razoumov et al., 2002; Maselli et al., 2003; Sokasian et al., 2003; Mellema et al., 2006; McQuinn et al., 2007; Trac & Cen, 2007; Semelin et al., 2007; Thomas et al., 2009). Recently, some of these simulations (e.g. Iliev et al. 2014) have been able to achieve the large dynamic range required to do statistics of the signal on scales comparable to the surveys. However, these simulations are computationally extremely expensive and it is therefore difficult to re-run the simulations using different values for the various mostly unknown reionization parameters.

A computationally much less expensive way of simulating the EoR 21-cm signal is provided by so-called semi-numerical simulations. These do not perform detailed radiative transfer calculations but rather consider the local average photon density (Furlanetto et al., 2004; Mesinger & Furlanetto, 2007; Zahn et al., 2007; Geil & Wyithe, 2008; Lidz et al., 2009; Choudhury et al., 2009; Alvarez et al., 2009; Santos et al., 2010). In addition to the conventional semi-numerical approach, recently Battaglia et al. (2013) have proposed an alternative method to simulate the 21-cm signal from the EoR, based on the bias between the underlying density field and the redshift of reionization. Although using somewhat different approaches, all of these different semi-numerical simulations are capable of simulating significantly large volumes of the Universe at reasonably low computational costs.

However, the approximations considered in these semi-numerical schemes may limit their ability to predict the redshifted 21-cm signal accurately. To address this issue, Zahn et al. (2011) performed a comparison between a set of semi-numerical and radiative transfer simulations of reionization, using the morphology of the resulting ionization maps and the spherically averaged real space H I power spectrum as metrics for the comparison. Their analysis shows that the prediction of the real space H I power spectrum using semi-numerical schemes differ from the corresponding radiative transfer simulations by less than 50% during most of the EoR at the length scales of interest for the present and future surveys.

Zahn et al. (2011) did not take into account the non-random distortions of the redshifted 21-cm signal due to peculiar velocities in their comparison. These so-called redshift space distortions play an important role in shaping the redshifted 21-cm signal and will introduce an anisotropy in the 3D power spectrum of the EoR 21-cm signal (Bharadwaj et al., 2001; Bharadwaj & Ali, 2004; Barkana & Loeb, 2005; Mao et al., 2012; Shapiro et al., 2013; Majumdar, Bharadwaj & Choudhury, 2013; Jensen et al., 2013), similar to the characteristic anisotropy present in the galaxy power spectrum (Kaiser, 1987). Mesinger et al. (2011) did compare the predictions of two semi-numerical schemes with a radiative transfer simulation using the redshift space 3D spherically averaged H I power spectrum. However they included the effect of redshift space distortions in these simulations in an approximate, perturbative fashion (similar to Santos et al. 2010), which itself may introduce an additional error of $\geq 20\%$ in the redshift space H I power spectrum (Mao et al., 2012).

In this paper we present a more thorough and rigorous comparison between the simulated H I 21-cm signal generated by a set of semi-numerical simulations and a radiative transfer simulation. Our comparison is threefold in nature: we compare these simulations in terms of their ability to reproduce the reionization history, the topology of the ionization field at different stages of EoR and various observable quantities of interest for a redshifted 21-cm survey to probe the EoR. We implement the redshift space distortions in our simulation in a more accurate manner than Santos et al. (2010) and Mesinger et al. (2011) by using the actual peculiar velocity fields. The observable quantities in redshift space that we focus on in this comparison are the variance of the brightness temperature fluctuations, the spherically averaged H I power spectrum and the ratios of various angular multipole moments of the H I power spectrum, which quantify the anisotropies in the signal due to redshift space distortions. Complementary to the variance of the brightness temperature fluctuations and the spherically averaged H I power spectrum, the angular multipole moments of the H I power spectrum in redshift space are expected to provide more information on the history as well as the intrinsic nature of the reionization (Majumdar, Bharadwaj & Choudhury, 2013).

In this work we compare two semi-numerical simulations with a radiative transfer simulation for hydrogen reionization. The case we compare is a simplified version of the reionization process in which we do not include several physical effects whose influence on reionization are currently not well established. We will mention these simplifications when we describe our numerical methods. In the comparison we address the following questions:

- How well and on which length scales can the semi-numerical schemes reproduce the reionization history of a radiative transfer simulation?
- How accurate are the morphologies of the ionization maps that are generated by these semi-numerical simulations?
- How important is it to take into account the effect of redshift space distortions accurately while generating the 21-cm signal using these semi-numerical methods?
- How accurately can different observables of the redshifted 21-cm signal (such as the variance, the spherically averaged power spectrum and the angular multipole moments of the power spectrum) be reproduced by these semi-numerical simulations?

[4] http://eor.berkeley.edu/
[5] http://21cma.bao.ac.cn/
[6] http://www.skatelescope.org/

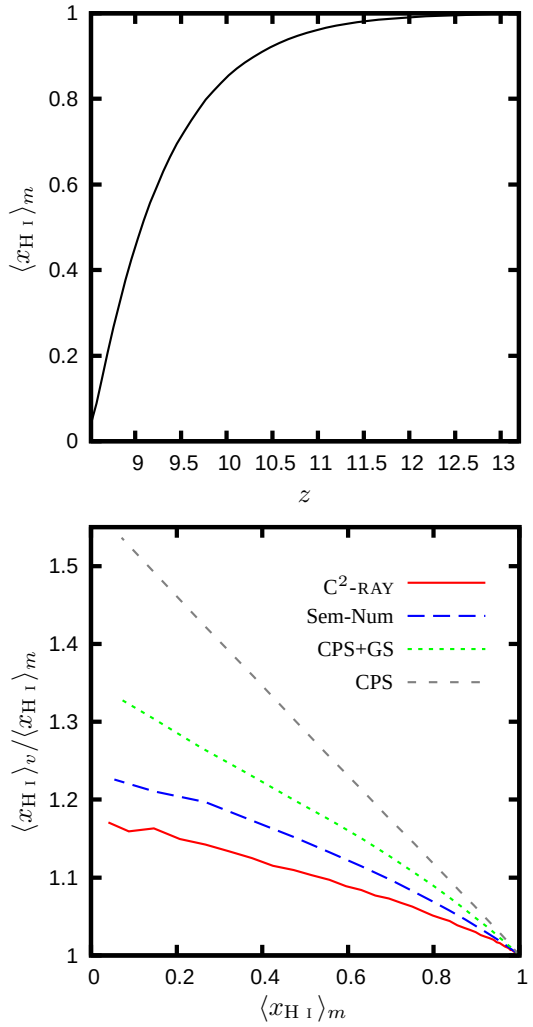

Figure 1. The top panel shows the reionization history through mass averaged neutral fraction for the radiative transfer simulation. Corresponding semi-numerical simulations are tuned to follow the same reionization history. The bottom panel shows the evolution of the ratio $\langle x_{\rm H\,I}\rangle_v/\langle x_{\rm H\,I}\rangle_m$ for all simulations of reionization considered here.

• Among the two semi-numerical methods discussed here, which one is the best considering its capability of generating the reionization history, morphology of the ionization maps and the observables of the 21-cm signal in redshift space and why?

Throughout this paper we present results for the cosmological parameters from WMAP five year data release $h = 0.7$, $\Omega_m = 0.27$, $\Omega_\Lambda = 0.73$, $\Omega_b h^2 = 0.0226$ (Komatsu et al., 2009).

The structure of the paper is as follows. In Section 2, we briefly describe the simulations used. In Section 3, we compare the reionization history as found by different simulations. Section 4 considers the morphology of the ionization fields generated by different simulations. In Section 5, we investigate the observable quantities as predicted by different simulations for a hypothetical redshifted 21-cm H I survey. We discuss our results and conclude in Section 6.

2 SIMULATIONS

2.1 N-body simulations

All of the reionization simulations discussed in this paper are based on a single N-body run, carried out using the CUBEP^{3}M code (Harnois-Déraps et al., 2013), which is based on PMFAST (Merz et al., 2005). CUBEP^{3}M uses a particle-particle-particle-mesh scheme, calculating short-range gravitational interactions directly between particles and long-range interactions on a grid. For performance reasons, this grid is split into a fine local grid and a coarser global grid. For the simulations considered here, we used a simulation volume of $(163\ {\rm Mpc})^3$ (comoving) with a fine grid consisting of 6144^3 cells. The number of N-body particles was 3072^3.

For each output from the N-body simulations, halos were identified using a spherical over-density method. This method encloses local density maxima in progressively larger spheres until the average density of the sphere goes below 178 times the global mean density. We allowed halos down to 20 particles, corresponding to $10^8\ M_\odot$. After constructing the halo lists, the N-body particles for each output were smoothed onto a grid with 256^3 cells to produce the density field. This N-body simulation was described in more detail in (Iliev et al., 2012).

2.2 Radiative Transfer simulations

For the radiative transfer simulations, we used C^2-RAY (Mellema et al., 2006)—"Conservative Causal Ray-tracing method". C^2-RAY works by tracing rays from all sources and iteratively solving the equation for the time evolution of the ionization fraction of hydrogen (x_i) as,

$$\frac{dx_i}{dt} = (1-x_i)(\Gamma + n_e C_H) - x_i n_e C \alpha_{\rm B}, \qquad (1)$$

where Γ is ionization rate, n_e is the density of free electrons, C_H is the collisional ionization coefficient, C is the so-called clumping factor and $\alpha_{\rm B}$ is the recombination coefficient. The clumping factor C is defined as $\langle n^2\rangle/\langle n\rangle^2$, where the average is taken over the volume resolution of the density field, in our case $163/256 = 0.64$ Mpc. This factor takes into account the effect of density variations below the resolution scale. This clumping factor depends on the density variations in the gas which will be both time- and position-dependent. There exist several approximate recipes to include the effect of subgrid clumping. However, since there is no consensus on the best way we take C to be 1 in our comparison, although we note that in reality it is expected to be larger than this.

Eq. (1) is solved by iterating over each cell and each source until convergence. By using the time-averaged Γ for each time step, C^2-RAY is able to use relatively large time-steps while still conserving photons (see Mellema et al. 2006).

In principle C^2-RAY can incorporate various kinds of source model. For this work, the sources from the N-body simulations described above were assigned ionizing fluxes $\dot{N}_\gamma$ proportional to the halo mass $M_{\rm h}$ as,

$$\dot{N}_\gamma = g_\gamma \frac{M_{\rm h}\Omega_{\rm b}}{(10\ {\rm Myr})\Omega_{\rm m} m_{\rm p}}, \qquad (2)$$

where $m_{\rm p}$ is the proton mass and g_γ is a source efficiency coefficient, which in effect depends on the star formation efficiency, the initial mass function and the escape fraction. In this particular simulation we have assumed that only those sources contribute to reionization which have mass $\geq 2.2\times10^9 M_\odot$ and we set $g_\gamma = 21.7$ for all of them. This simulation was previously described in Iliev et

al. (2012) as "L3". We selected this simulation since it does not use any suppression of sources, a process which is not included in the semi-numerical methods we use here. This is another simplification we introduce in order to compare the radiative transfer and semi-numerical methods at the more basic level without the introduction of subgrid physics whose influence on reionization is currently not well established.

The reionization history for this model is illustrated through the evolution of the mass averaged neutral fraction ($\langle x_{\rm H\,I}\rangle_m$, also represented by $\bar{x}_{\rm H\,I}$ for convenience in the rest of the paper) in the top panel of Figure 1.

2.3 Semi-numerical simulations

C^2-RAY and similar kinds of radiative transfer algorithms are capable of generating an accurate reionization topology and history since they take into account the ionization and recombination processes (eq. [1]) along the path of each individual photon. However, to achieve this level of precision they require huge amounts of computational time (hundreds of thousands of core hours). Thus, it would be very expensive to explore the mostly unknown parameter space of possible reionization models using this kind of simulations. Furthermore, most of the present and upcoming radio interferometric reionization surveys (including the humongous SKA) will not be sensitive enough to map the H I distribution from this epoch with a precision and resolution comparable to that of the simulations. These limitations of the radiative transfer simulations as well as the poor sensitivity of the present and future EoR 21-cm surveys together have motivated the development of approximate semi-numerical methods to simulate the redshifted 21-cm signal from EoR. These approximate methods are expected to simulate the H I 21-cm signal from this epoch accurately enough for the length scales to which the present and upcoming 21-cm surveys will be sensitive, at a very nominal computational cost. They can simulate a reasonable volume of the universe (comparable to the survey volume of LOFAR or SKA) in a few minutes of computational time on a single processor with considerably less memory consumption (few gigabyte of RAM). If semi-numerical simulations are accurate enough in predicting the redshifted 21-cm signal from EoR, one can achieve almost a five orders of magnitude gain in computational time compared to a radiative transfer simulation.

Most of the conventional semi-numerical methods of simulating EoR are based on comparing the average number of photons in a specific volume with the average number of neutral hydrogen present in that volume. This is the basic principle of the excursion-set formalism developed by Furlanetto et al. (2004). We discuss two different approaches of implementing it in the following sections. One important common feature of the two semi-numerical simulations discussed here is that the ionization map generated by them at each redshift is dependent only on the matter distribution or the matter and source distribution at that specific redshift. Due to this it is possible to generate the ionization maps at several redshifts simultaneously (or in parallel) using these simulations.

2.3.1 Semi-numerical simulation with halos (Sem-Num)

The first of the semi-numerical methods we use here is based on the excursion-set formalism of Furlanetto et al. (2004) and similar to Zahn et al. (2007), Mesinger & Furlanetto (2007), Choudhury et al. (2009) and Santos et al. (2010). Here we assume that the halos are the sites where the ionizing photon emitting sources were formed. To date, little is known about the high redshift photon sources and the characteristics of their radiation, so this method assumes that the total number of ionizing photons contributed by a halo of mass $M_{\rm h}$ is

$$N_\gamma(M_{\rm h}) = N_{\rm ion}\frac{M_{\rm h}\Omega_{\rm b}}{m_{\rm p}\Omega_{\rm m}} \tag{3}$$

where $N_{\rm ion}$ is a dimensionless constant, which effectively represents the number of photons entering in the IGM per baryon in collapsed objects. In this paper we have assumed that $N_\gamma(M_{\rm h})$ is proportional to the halo mass $M_{\rm h}$ but in principle one can assume any functional form for $N_\gamma(M_{\rm h})$. This particular source model (eq. [3]) is thus similar to that of C^2-RAY (eq. [2]). The assumptions regarding the source model play a crucial role in the resulting ionization and brightness temperature fields from a semi-numerical simulation, as will become more clear in the next few sections.

Once the locations and masses of the halos are known and a functional form for $N_\gamma(M_{\rm h})$ has been assigned, the ionizing photon field can be constructed. To construct the ionization field, we estimate the average number density of photons $\langle n_\gamma(\mathbf{x})\rangle_R$ within a spherical region of radius R around a point $\mathbf{x}$ and compare it to the corresponding spherically averaged number density of neutral hydrogen $\langle n_{\rm H}\rangle_R$. The radius of this smoothing region is then gradually increased, starting from the grid cell size ($R_{\rm cell}$) and going up to a certain $R_{\rm max}$, which is determined by the assumed mean free path of the photon at the concerned redshift. We consider the point $\mathbf{x}$ to be ionized[7] if the condition

$$\langle n_\gamma(\mathbf{x})\rangle_R \geq \langle n_{\rm H}\rangle_R(1+\bar{N}_{\rm rec}) \tag{4}$$

is satisfied for any smoothing radius R, where $\bar{N}_{\rm rec}$ is the average number of recombinations[8] per hydrogen atom in the IGM. Note that various other unknown parameters *e.g.* star formation efficiency within halos, number of photons per unit stellar mass, the photon escape fraction, helium weight fraction, as well as the factor $(1+\bar{N}_{\rm rec})$ can be absorbed within the definition of $N_{\rm ion}$ and we do so in this work. In other words, in this description the effect of recombinations can be compensated by making the sources more efficient. It also means that the effect of recombinations is here taken to be uniform over the whole volume, although in reality it will be position-dependent. Because of this, we have chosen the clumping factor in eq. (1) to be 1, so as to make the treatment of recombinations more similar between the semi-numerical and numerical methods.

We apply periodic boundary conditions when calculating the ionization field. Points where the above ionization condition is not satisfied, are given an ionization fraction equal to $\langle n_\gamma(\mathbf{x})\rangle_{R_{\rm cell}}/\langle n_{\rm H}\rangle_{R_{\rm cell}}$. This approximately takes into account the H II regions not resolved by the resolution of the simulation (Geil & Wyithe, 2008). Finally, we tune the value of $N_{\rm ion}$ in such a way that we achieve the same evolutionary history for $\langle x_{\rm H\,I}\rangle_m$, as C^2-RAY (see top panel of Figure 1). Hereafter we refer to this method as "Sem-Num".

[7] The main difference between Mesinger & Furlanetto (2007) and this approach is the following. In our simulation we assume that only the central pixel of the smoothing sphere is ionized when the ionization condition is satisfied, whereas in Mesinger & Furlanetto (2007) it is assumed that the entire region inside the smoothing sphere is ionized. In this sense, our method of flagging ionized cells is similar to what is done in Mesinger et al. (2011).

[8] It is also possible to incorporate a self-shielding criterion in this simulation based on a density dependent recombination scheme (eq. [15] of Choudhury et al. 2009), which we do not consider in this work.

2.3.2 Conditional Press-Schechter (CPS and CPS+GS)

The second semi-numerical method we consider here is based on the conditional Press-Schechter formalism initially proposed by Bond et al. (1991) and Lacey & Cole (1993) and later modified by Barkana & Loeb (2004, 2008). Unlike the previous semi-numerical simulation, where the halos are the locations of the ionizing sources, this method is solely based on the underlying matter density field. According to this scheme the collapsed fraction at a redshift z within a region of size R depends on the mean overdensity of that region $\bar{\delta}_R$ as

$$f_{\rm coll} = \frac{\bar{f}_{\rm ST}}{\bar{f}_{\rm PS}} \, {\rm erfc} \left[\frac{\delta_c(z) - \bar{\delta}_R}{\sqrt{2\left[\sigma^2(R_{\rm min}) - \sigma^2(R)\right]}} \right] , \qquad (5)$$

where $R_{\rm min}$ is the radius that encloses the mass $M_{\rm min}$ at average density $\bar{\rho}$, $\delta_c(z)$ is the critical over density required for spherical collapse and has the redshift dependence $\delta_c(z) = 1.686/D(z)$, $D(z)$ is the linear growth factor, $\sigma^2(R)$ is the linear theory rms fluctuation of the density on scale R, $\bar{f}_{\rm ST}(z, R_{\rm min})$ is the mean Sheth-Tormen collapsed fraction with the normalization of Jenkins et al. (2001) and $\bar{f}_{\rm PS}(z, R_{\rm min}, R)$ is the mean Press-Schechter collapsed fraction estimated from the density field at redshift z after being smoothed over a length scale of size R. We set $M_{\rm min} = 2.2 \times 10^9 M_\odot$ at all redshifts, to keep it consistent with the minimum halo mass used in the other simulations of reionization considered in this paper. One advantage of this simulation method over any halo based simulation scheme (semi-numerical or radiative transfer) is that it is not restricted by the particle mass resolution required to identify the atomically cooling halos ($M_{\rm min} \sim 10^8 M_\odot$) or even molecularly cooling halos ($M_{\rm min} \sim 10^6 - 10^8 M_\odot$). This allows us to include the contribution from atomically and molecularly cooling halos without detecting them individually. These sources could contribute substantially to the reionization process. We note, however, that for a given resolution, the CPS value for $f_{\rm coll}$ is not identical to the numerical one.

For a specific smoothing scale R, a point is considered to be ionized if the collapsed fraction calculated for a smoothing region of size R around it is more than the inverse of the ionizing efficiency ζ

$$f_{\rm coll} \geq \zeta^{-1} . \qquad (6)$$

Similar to the $N_{\rm ion}$ in the previous simulation, various parameters of reionization can be incorporated into ζ. This simulation model is similar to the models of Zahn et al. (2005); Alvarez et al. (2009); Zahn et al. (2011); Mesinger et al. (2011). In this scheme, by default, uniform or no recombination[9] is assumed for every part of the density field. In an earlier work, Zahn et al. (2011) have reported that the ionization map shows a better match with the radiative transfer simulations when the smoothing is done with a sharp k-space filter instead of a spherical top hat filter. However, we observe that both the spherical top hat and the sharp k-space filter produce very similar ionization maps in this case (when compared in terms of their bubble size distribution and power spectrum). In this work we choose to use a sharp k-space filter for the smoothing of the density field as it is expected to keep the photon number conserved in comparison to the spherical top hat filter (Zahn et al., 2007).

[9] Recently Sobacchi & Mesinger (2014) have developed a model to implement a density dependent recombination scheme which can be combined with this simulation model. We do not consider it in this work.

Simulation	Density field used	Halos used as sources	Ionization field obtained by
C^2-RAY	N-body	Yes	Radiative transfer
Sem-Num	N-body	Yes	Excursion-set based
CPS	N-body	No	Excursion-set based
CPS+GS	N-body+GS	No	Excursion-set based

Table 1. The major characteristics of the different simulations considered here.

Irrespective of what filter we use, this simulation technique tends to produce a much stronger "inside-out" reionization than other two models (an initial indication of this can be seen in the bottom panel of Figure 1). This leads to the production of more small scale ionized regions at any stage of reionization. The density field used in Mesinger et al. (2011) was constructed at a very high redshift using Zel'dovich approximations and then extrapolated to redshift z. The matter distribution in such a density field is expected to be slightly more diffuse (or less clustered) in nature than the one obtained using an N-body simulation, as in our case. This inherent diffuse nature of the density field probably prevents the production of a large number of small scale ionized regions. To generate a similar sort of diffused density field, we convolve the N-body density field with a Gaussian filter of width ≈ 2 Mpc (equivalent to the size of 3 grid cells in this case). The collapsed fraction is then estimated from this density field following eq. (5). As we will see in the following sections, this treatment makes the output from this simulation more similar to the other two discussed here. To achieve the same $\langle x_{\rm H\,I} \rangle_m$ evolution as that of the C^2-RAY, we adjust the value of ζ. Hereafter we refer to this simulation method as "CPS+GS". For most of our comparison analysis in this paper we have used these Gaussian-smoothed density fields for CPS+GS but we have also used unsmoothed density fields (hereafter referred to as "CPS") for some test comparisons.

In Table 1, we briefly summarize the major characteristics of all the simulations discussed here.

3 RECONSTRUCTION OF THE REIONIZATION HISTORY

As mentioned in the previous section, the ionization field produced by these two semi-numerical simulations at a specific redshift will not have any memory of the ionization field at an earlier redshift. However, it is possible to chronologically follow the reionization history in these semi-numerical simulations by sequentially producing ionization maps using the previously produced, higher-redshift, maps as input. This will, however, slow down the semi-numerical schemes by not allowing them to generate the ionization maps at a number of redshifts simultaneously (or in parallel).

In this work, we have run our semi-numerical schemes following the usual convention (*i.e.* we have not followed the ionization state of each grid point chronologically to determine its ionization state at a later redshift). Generally, the values of $N_{\rm ion}$ or ζ are adjusted in such a way that these simulations approximately produce the same $\langle x_{\rm H\,I} \rangle_m$ or $\langle x_{\rm H\,I} \rangle_v$ evolution as found in radiative transfer simulations. We adopt the same approach in this work. However, to interpret the EoR redshifted 21-cm signal from future surveys with these approximate simulations, they should be capable of reproducing the reionization history with a certain acceptable level

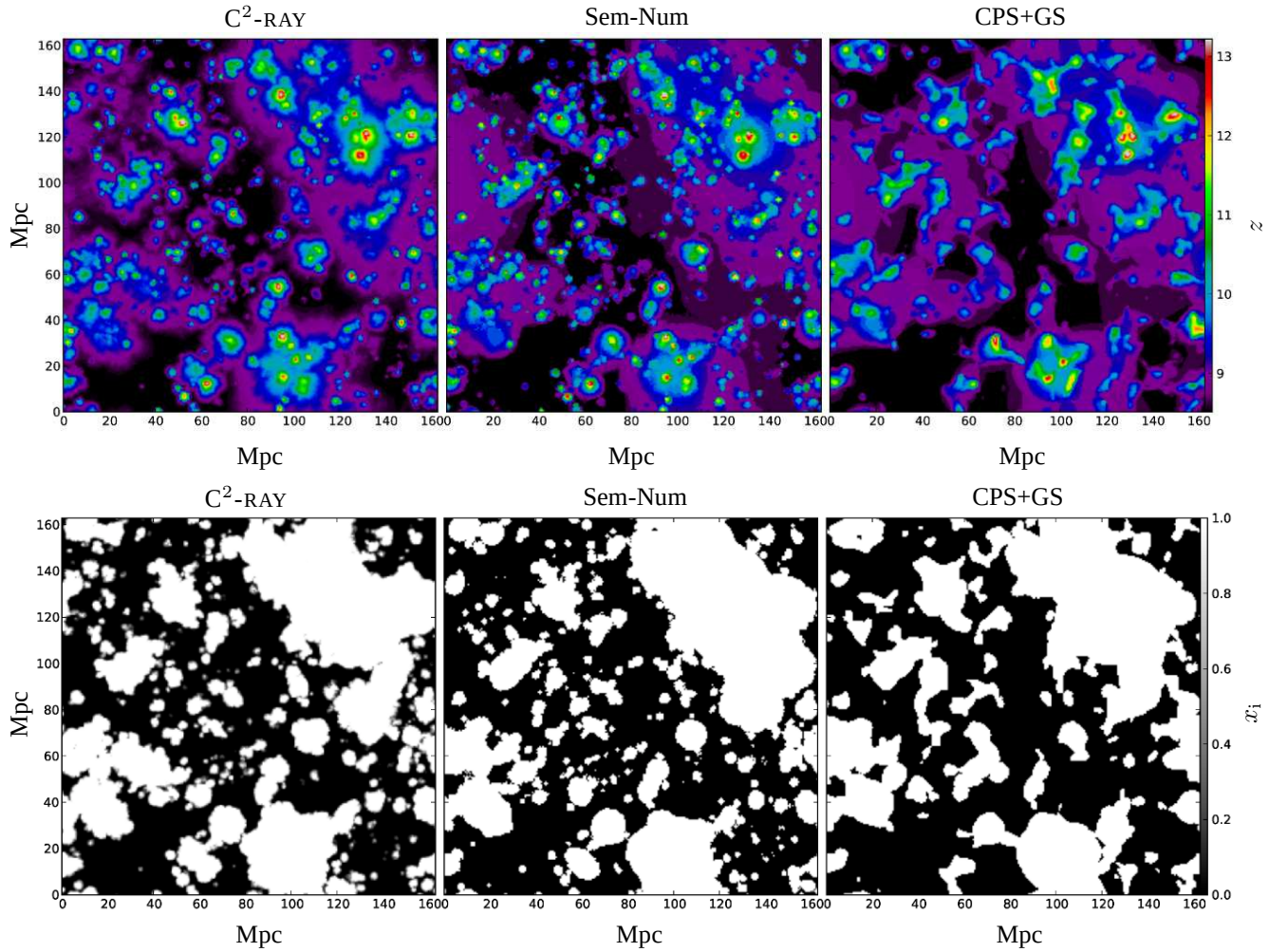

Figure 2. *Top panel:* the redshift of reionization in each individual cell for three different simulations. *Bottom panel:* the state of ionization in three different simulations when the reionization was half way through ($z = 9.026$). The thickness of each slice is 0.64 Mpc.

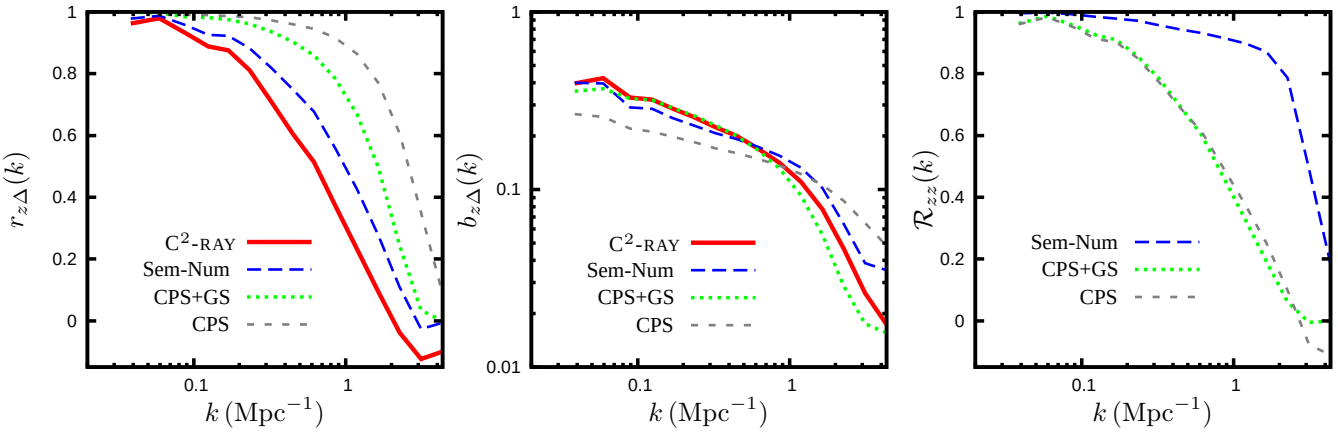

Figure 3. First two panels from left show the cross-correlation $r_{z\Delta}(k)$ between the density field at the mid-point of reionization ($z = 9.026$) and the redshift of reionization field and the bias $b_{z\Delta}(k) = \sqrt{P_{zz}(k)/P_{\Delta\Delta}(k)}$ between the same quantities for different simulations, respectively. The third right most panel shows the cross-correlation $\mathcal{R}_{zz}(k)$ between the redshift of reionization fields for C^2-RAY and the same from different semi-numerical simulations.

of accuracy. In this section we explore up to what extent they can reliably mimic the reionization history.

We first study the evolution of the volume-averaged neutral fraction produced by different simulations. As mentioned earlier, both of the semi-numerical simulations are tuned to produce the same evolution for the mass-averaged neutral fraction ($\langle x_{\rm H\,I}\rangle_m$) as that of the C^2-RAY. However, due to the differences in their approach, the evolution of $\langle x_{\rm H\,I}\rangle_v$ is not necessarily the same for the four simulations. The bottom panel of Figure 1 shows the ratio $\langle x_{\rm H\,I}\rangle_v/\langle x_{\rm H\,I}\rangle_m$ as a function of $\langle x_{\rm H\,I}\rangle_m$ for the four different simulations discussed earlier. It is clear from this plot that at almost any stage of reionization (except the very beginning), $\langle x_{\rm H\,I}\rangle_v$ is always smaller for C^2-RAY than for the two semi-numerical simulations. This difference gradually increases as reionization progresses. This implies that less volume is ionized in case of the two semi-numerical simulations with respect to C^2-RAY to achieve the same mass averaged ionization fraction. This further implies that the ionization maps in semi-numerical simulations follow the density field more closely than the radiative transfer simulation (we will elaborate on this point further in the following sections). Among the two semi-numerical schemes, CPS+GS has a higher value of $\langle x_{\rm H\,I}\rangle_v/\langle x_{\rm H\,I}\rangle_m$ than Sem-Num at any stage and this difference goes up to approximately 10% at the very late stages of reionization. When the Gaussian smoothing of the density field is not done in CPS, the difference between Sem-Num and CPS can go up to approximately 30%.

Next, we show how well these semi-numerical simulations are able to reconstruct the history at the level of each individual grid cell. To do so, we have saved the redshift of reionization of each grid point for four different simulations. We have used an ionization threshold of $x_{th} \geq 0.5$ to identify a cell as ionized. The top panel of Figure 2 shows one slice of the simulation box with a colour coded map for redshift of reionization for the three different schemes. A simple visual inspection of this image along with the ionization state of the same slice at the mid point of reionization (bottom panel of Figure 2) suggest that the reionization history reproduced by Sem-Num resembles that of the C^2-RAY simulation more than CPS+GS does. The redshift map of CPS+GS looks smoother than the other two simulations. This is a clear signature of the more diffuse matter distribution that was used in CPS+GS. We find that the reionization redshift map for Sem-Num is highly correlated to that of the C^2-RAY. The correlation coefficient between these two maps (right most panel in Figure 3) has a value ≥ 0.9 for length scale range $k \leq 1.0\,{\rm Mpc}^{-1}$. The same correlation between CPS+GS and C^2-RAY is ≥ 0.4 for $k \leq 1.0\,{\rm Mpc}^{-1}$.

We estimate the bias and cross-correlation between the reionization redshift and the matter density field to quantify how the reionization history is related to (or rather controlled by) the underlying matter distribution. We define the fluctuations in the redshift of reionization field as $\delta_z(\mathbf{x}) = \{[1+z(\mathbf{x})] - [1+\bar{z}]\}/[1+\bar{z}]$ and similarly for a density field at a specific redshift as $\delta = [\rho(\mathbf{x}) - \bar{\rho}]/\bar{\rho}$, where $\bar{z}$ and $\bar{\rho}$ are the means of the corresponding reionization redshift and the density field respectively. Thus the bias and cross-correlation between these two fields in Fourier space can be defined as $b_{z\Delta}(k) = \sqrt{P_{zz}(k)/P_{\Delta\Delta}(k)}$ and $r_{z\Delta}(k) = P_{z\Delta}(k)/\sqrt{P_{zz}(k)P_{\Delta\Delta}(k)}$, respectively. The quantities P_{zz} and $P_{\Delta\Delta}$ are the power spectrum of the field δ_z and δ respectively and $P_{z\Delta}$ is the cross-power spectrum between these two fields.

We calculate the bias factor and the cross-correlation between the reionization redshift field and the matter density field at approximately the mid point of reionization (*i.e.* at $z = 9.026$ when $\langle x_{\rm H\,I}\rangle_m \simeq 0.5$). The central panel in Figure 3 shows the bias $b_{z\Delta}(k)$ for the four different simulations. In all four, the bias between redshift and density is highest at the largest scale and gradually decreases at smaller scales. The bias estimated from Sem-Num and CPS+GS are in very good agreement with that of C^2-RAY (less than 5% difference) for $k \leq 1.0\,{\rm Mpc}^{-1}$, whereas the bias estimated from CPS (in which Gaussian smoothing of the density field is not done) is lower than that of C^2-RAY ($\sim 30-50\%$ less) in the same length scale range. We find that the reionization history in the case of CPS+GS is more strongly correlated with the density field ($r_{z\Delta} \geq 0.8$ for $k \leq 1.0\,{\rm Mpc}^{-1}$; left most panel in Figure 3) compared to C^2-RAY and Sem-Num ($r_{z\Delta} \geq 0.3$ and ≥ 0.5, respectively for the same k range). The cross-correlation between same two fields in case of CPS is even higher ($r_{z\Delta} \geq 0.9$ for $k \leq 1.0\,{\rm Mpc}^{-1}$).

This statistical analysis suggests that Sem-Num is capable of producing a more reliable reionization history compared to CPS+GS or CPS at the length scales corresponding $k \leq 1\,{\rm Mpc}^{-1}$. The estimated cross-correlation $r_{z\Delta}$ also suggests that for CPS+GS and CPS reionization is more strongly correlated with the density field than the other two schemes.

Battaglia et al. (2013) constructed an empirical model of reionization by extrapolating the bias $b_{z\Delta}(k)$ and cross-correlation $r_{z\Delta}$ of a radiative transfer simulation. We find that even when the history of reionization is not followed chronologically at the level of individual grid cells, a semi-numerical simulation like Sem-Num is still capable of generating the same bias and cross-correlation as that of the radiative transfer simulation at length scales relevant for the present and upcoming EoR 21-cm experiments. The main difference between Sem-Num and CPS+GS or CPS is in the source model. The source model of Sem-Num (eq. [3]) is very similar to that of the C^2-RAY (eq. [2]). We can thus safely say that a semi-numerical scheme can reliably reproduce the reionization history of a radiative transfer simulation when a similar source model is used in it.

4 COMPARISON OF THE MORPHOLOGY OF THE IONIZATION MAPS

The evolution of the morphology of the ionization field directly controls the evolution of the redshifted H I 21-cm signal. In this section we use a few different statistical measures to analyze and quantify the morphology of the ionization maps generated by the three different simulation methods. Some of these morphological similarities can be seen easily from a rough visual inspection of the ionization maps (see bottom panels of Figure 2 and brightness temperature[10] maps of Figure 9). However, such a visual inspection will also reveal some of their differences. In all three simulation methods discussed here, the ionized regions essentially follow the distribution of the ionizing sources (*i.e.* the distribution of the halos or the high density peaks) at the very early stages of reionization and are small in size. As the time progresses, the H II regions gradually get larger in size and start merging with each other. At the very late stages of reionization the ionization fronts start progressing into the low density regions and finally, almost the entire IGM is ionized.

Among the two semi-numerical schemes, Sem-Num produces

[10] The brightness temperature is directly proportional to the neutral fraction, so these brightness temperature maps have a one-to-one correspondence with the ionization maps. Note that the brightness temperature maps shown here are in redshift space.

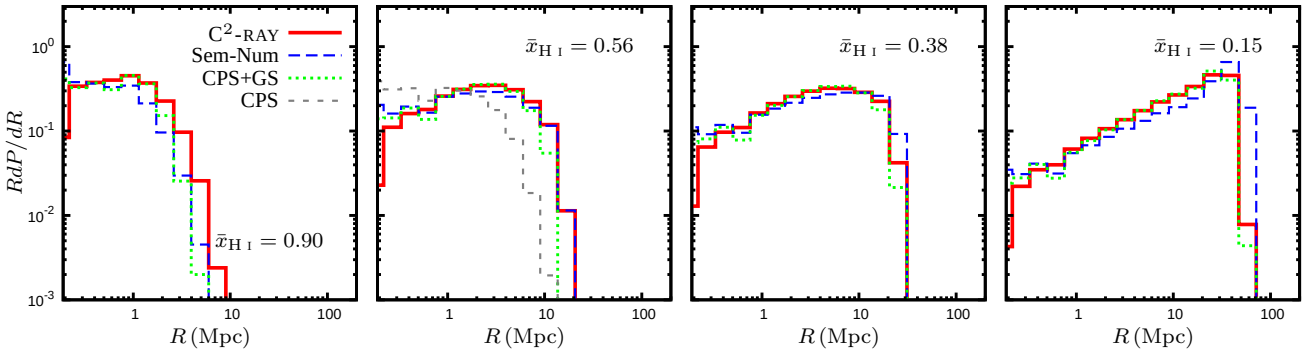

Figure 4. The spherical average bubble size distribution at four representative values of $\bar{x}_{\rm H\,I}$. We show the distribution for CPS at $\bar{x}_{\rm H\,I} = 0.56$ only, to illustrate its marked difference from C^2-RAY.

an ionization map which is visually more similar to that of C^2-RAY. On the other hand, the H II regions in the ionization maps produced by CPS+GS appears to be more connected than the other two simulations. This is again a indication of the fact that the ionization maps are more strongly correlated with the density fields in case of CPS+GS than for the other two simulations. We investigate this and other differences in further details in the following sections using various statistical measures.

4.1 Bubble Size Distribution

The bubble size distribution is one of the basic measures of the morphology of the ionization fields. However, due to the complex three-dimensional morphology of the ionized regions, no unique method exists that captures this distribution. Instead, several different methods exist, which each show different properties of the size distribution of ionized regions (Friedrich et al., 2011). Here we compare the results of our three simulations using three of these, namely the spherical average method, the friends-of-friends bubble size distribution and the (spherically averaged) power spectrum of the ionization field.

4.1.1 Spherical average method

First we use a spherical average technique, similar to Zahn et al. (2011) and Friedrich et al. (2011), to estimate the bubble size distribution from different simulations. Figure 4 shows the bubble radius distribution (RdP/dR) for the three different simulations at four representative stages of reionization. The distribution have some characteristics which are common to all three simulations. During the early stages of EoR all three simulations produce relatively smaller bubbles, the maximum bubble size is restricted to $R \leq 10\,{\rm Mpc}$ and the peak of the distribution appears around $R \simeq 1\,{\rm Mpc}$. As reionization progresses the peak of the distribution gradually shifts towards larger bubble size and finally reaches $R \simeq 50\,{\rm Mpc}$ at the end stages of EoR.

Except at very early stages of EoR all three simulations show good agreement in their spherical average bubble size distribution throughout the history of reionization for most of the length scales. There is almost no difference between the two semi-numerical schemes (*i.e.* Sem-Num and CPS+GS). During very early stages of EoR ($\bar{x}_{\rm H\,I} = 0.90$), distribution for both semi-numerical simulations differ slightly from C^2-RAY for larger bubble radii ($R \sim 2-10\,{\rm Mpc}$) and for very small bubble size (comparable to the grid size). Except this during all other stages of reionization, C^2-RAY differs from both semi-numerical simulations only at very small length scales.

For comparison we also show the bubble size distribution for CPS (without Gaussian smoothing) at the stage when $\bar{x}_{\rm H\,I} = 0.56$. We find that the distribution in this case is significantly different even from CPS+GS at both large and small scales ($R \sim 10\,{\rm Mpc}$). The RdP/dR appears to be biased towards small scales, whereas excess small scale bubble production is compensated by very low bubble population at the large scales. This essentially indicates a much stronger "inside-out" reionization than CPS+GS in this case.

Zahn et al. (2011) obtained similar results with this technique. They found that, due to its over-connected nature, FFRT (equivalent of CPS+GS in our case) produces more large scale bubbles and fewer small scale bubbles compared with a radiative transfer simulation. The other semi-numerical scheme (Mesinger & Furlanetto, 2007) in their analysis which is similar to Sem-Num, also shows similar behaviour. This is probably due to the fact that contrary to Sem-Num, which identifies only the central pixel of the smoothing sphere as ionized when eq. (4) is satified, Mesinger & Furlanetto (2007) identifies the entire smoothing sphere to be ionized. This leads to the production of more large scale ionized regions. Also, Zahn et al. (2011) have tuned their semi-numerical schemes so as to achieve the same evolution of the volume-averaged neutral fraction as that of the radiative transfer simulations, whereas we have compared different simulations at the level of same mass-averaged neutral fraction. This in addition may enhance these small discrepancies. In addition to this we would also like to note that previous studies by Friedrich et al. (2011) have shown that the spherical average technique tends to wash out some of the complicated features in the bubble shape (most of which are essntially non-spherical) and produce smoother distributions. We confirm this behaviour here as well.

4.1.2 Friends-of-friends analysis

We next use a friends-of-friends (FoF) algorithm, as in Iliev et al. (2006) and Friedrich et al. (2011), to identify ionized regions from our simulations. In this method, for a gridded ionization map, two adjacent grid cells are considered to be part of the same ionized region if they fulfill the same condition. Here, we use an ionization threshold condition of $x_{th} \geq 0.5$. One important characteristic of this method is that it does not presume anything about the shape of

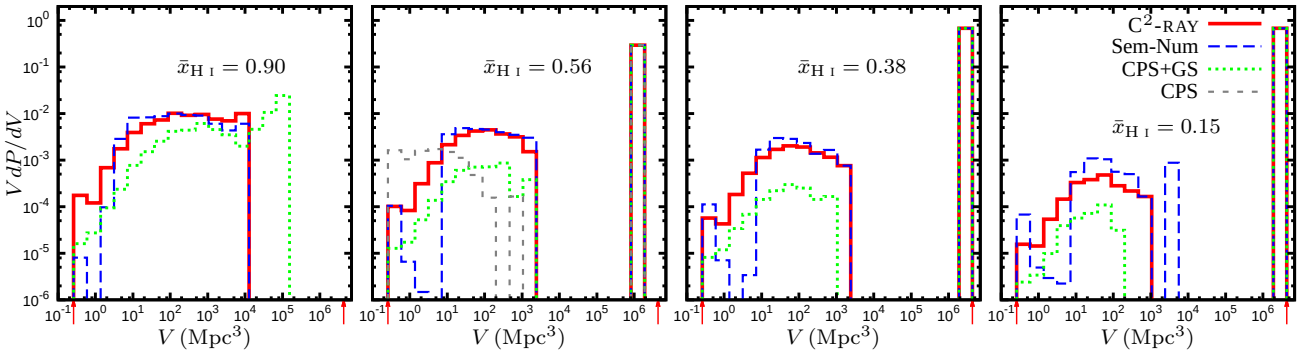

Figure 5. The FoF bubble size distribution at four representative values of $\bar{x}_{\rm H\,I}$. The red arrows mark the cell and the box volume. We show the distribution for CPS at $\bar{x}_{\rm H\,I} = 0.56$ only, to illustrate its marked difference from C^2-RAY.

the ionized regions and literally allows connected ionized regions of any shape to be identified.

For a field consisting of continuous ionization fractions, such as produced by a numerical simulation, the results of this method depend on the choice for the ionization threshold, as shown in Friedrich et al. (2011). For the semi-numerical simulations, in which the ionization fraction is either 0 or 1 the FoF is defined uniquely. However, one may wonder if even in this case the results are very sensitive to small scale features, either connecting or not connecting two ionized regions. We tested this by performing the same analysis after applying a Gaussian or a spherical smoothing filter with the effective width of 3 simulation cells to the ionization fields. We found that this procedure, as expected, does reduce the number of small bubbles. However, it does not significantly affect the distribution at intermediate and large length scales. We therefore conclude the FoF statistics for volumes above $100\,{\rm Mpc}^3$ to be a robust result and not sensitive to small scale effects.

Figure 5 shows the bubble volume distribution (VdP/dV) for the three simulations at four representative stages of reionization. The distributions have some characteristics which are common to all three simulations. One of the main features is that the distributions are not continuous except at the very early stages of reionization ($\bar{x}_{\rm H\,I} \geq 0.90$). Another distinct feature is that once the early phase of reionization is over there is one connected large H II region which is comparable to the volume of the simulation box ($\sim 10^6\,{\rm Mpc}^3$). The rest of the H II regions are much smaller ($\sim 0.26 - 10^4\,{\rm Mpc}^3$) in size and have an almost continuous distribution for all simulations.

The bubble size distribution for Sem-Num is quite similar to that of C^2-RAY during almost the entire period of reionization. The only disparity in the bubble size distribution between the two appears at relatively small length scales. The number of bubbles is notably lower in the Sem-Num simulation for the volume range $\sim 1 - 10\,{\rm Mpc}^3$ than for C^2-RAY. For the smallest volume bin this number is slightly larger than C^2-RAY.

In contrast, CPS+GS produces clearly quite different results. This is especially evident at the intermediate and smaller length scales where it produces significantly fewer bubbles than C^2-RAY and Sem-Num do. This is consistent with our previous observation of the ratio $\langle x_{\rm H\,I}\rangle_v/\langle x_{\rm H\,I}\rangle_m$ in Figure 1. We observe that at all stages of the EoR $\langle x_{\rm H\,I}\rangle_v/\langle x_{\rm H\,I}\rangle_m$ is higher for CPS+GS than for the other two simulation, *i.e.* the volume fraction of H I is always more than the mass fraction of H I in CPS+GS. This implies that reionization is more biased around high density regions in CPS+GS than the other two schemes (more "inside-out").

For the purpose of comparison here also we show the bubble size distribution for CPS (without Gaussian smoothing) at the stage when $\bar{x}_{\rm H\,I} = 0.56$. We find that the distribution in this case is markedly different even from CPS+GS. The VdP/dV is significantly biased towards small scales, whereas excess small scale bubble production is compensated by almost zero bubble population at the intermediate scales. This indicates a much stronger "inside-out" reionization than CPS+GS in this case. At the same reionization state CPS+GS generates considerably fewer bubbles at the smallest scales (comparable to the cell volume). This is probably due to the fact that the density field in case of the CPS+GS is more diffused which prevents the over-production of very small ionized regions.

Furthermore, the way the two semi-numerical simulations treat recombinations can also affect the bubble size distributions. In both of the semi-numerical methods we assume a uniform recombination rate throughout the IGM, which can be considered to be equivalent to having no recombinations at all (as they can be effectively absorbed in the source efficiency parameter $N_{\rm ion}$ or ζ). This inaccurate implementation of recombinations can lead to the discrepancy in bubble size distribution. However, we will see in the following sections that this does not drastically affect the simulated 21-cm signal from these semi-numerical simulations. This is because the 21-cm signal is a product of neutral fraction and density fluctuations. During the early stages of the EoR it is the density fluctuations which plays a dominating role over the fluctuations in $x_{\rm H\,I}$, thus reduces the effect of differences in the ionization maps at this stage.

4.1.3 *Power spectrum*

The power spectrum of the ionization field ($P_{xx}(k)$) is also a measure of the H II bubble size distribution. It measures the amplitude of fluctuations in the ionization field at different length scales. It also directly contributes to the redshift space 21-cm H I power spectrum, which is a major observable quantity for the present and the future EoR experiments. Figure 6 shows the power spectrum of the ionization maps at four representative stages of the EoR. The power spectra of the ionization field also have some features common to all three simulations of reionization considered here. Similar to the bubble size distribution, the peak of the power spectrum gradually shifts from small to large length scales (*i.e.* from large to small k modes) and its amplitude also increases as reionization progresses

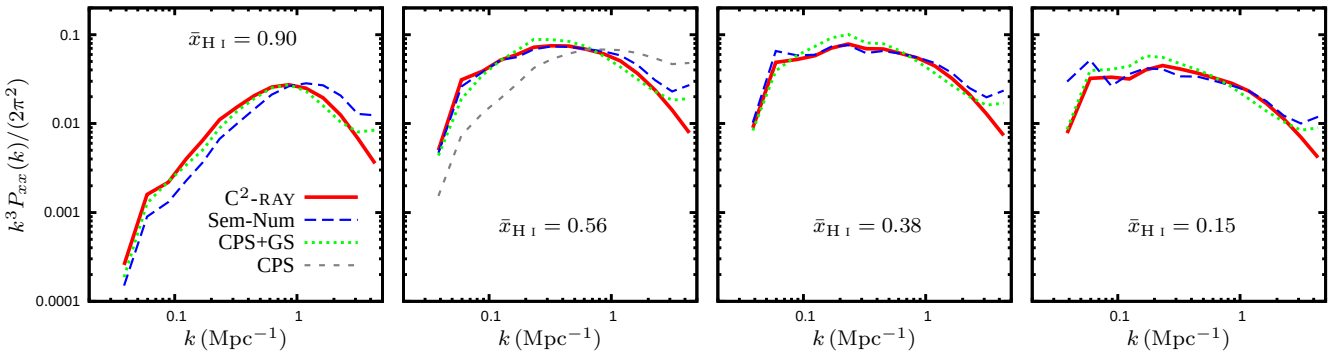

Figure 6. The power spectrum of the ionization field $P_{xx}(k)$ at four representative neutral fraction values. We show the power spectrum for CPS at $\bar{x}_{\rm H\,I} = 0.56$ only, to illustrate its marked difference from C^2-RAY.

(up to $\bar{x}_{\rm H\,I} \geq 0.5$). This indicates the gradual growth and merger of the H II regions with time. Finally, at the very late stages of the EoR, when most of the volume is ionized, the power spectrum becomes almost flat and there is a significant decrement in its overall amplitude as well.

The differences in power spectrum between the three different simulations is relatively small. At the very early stages of reionization, Sem-Num produces less power at almost all scales (except very small scales) compared with the other two simulations, whereas CPS+GS is in good agreement with C^2-RAY at this stage. At the intermediate and late stages of the EoR, Sem-Num replicates the power spectrum from C^2-RAY much better than CPS+GS, except at the very small length scales. However at the smallest length scales, Sem-Num always produces more power than the other two simulations. This is due to the fact that it produces more small scale bubbles than the other two schemes, which is also evident in the bubble size distributions (Sect. 4.1). Overall during the intermediate stages of EoR, $P_{xx}(k)$ for Sem-Num lies within 15% of that of C^2-RAY, whereas for CPS+GS it lies within 25% of that of C^2-RAY (for $k \leq 2.0\,{\rm Mpc}^{-1}$). As reported in previous studies (Zahn et al., 2011; Friedrich et al., 2011), we also note that the power spectrum analysis essentially produce similar results as that of the spherical average technique.

For comparison we also show the power spectrum from CPS when reionization is almost half way through ($\bar{x}_{\rm H\,I} \approx 0.56$). We observe that as we do not use a diffused density field in CPS, it produces more small H II regions than CPS+GS. This means more power at small scales and less power at large scales, which changes the shape of the power spectrum significantly. In a similar analysis, Zahn et al. (2011) find that their FFRT scheme produces more power at both largest and smallest scales than the radiative transfer schemes. This we do not encounter in case of CPS+GS. Due to the significant differences observed in the history, bubble size distribution and power spectrum between CPS (without Gaussian smoothing) and other simulations, we drop it from our comparison analysis here onwards.

4.1.4 Comparison of bubble size distribution results

From these three methods for bubble size distributions we conclude that the two methods which do not take into account connectivity, namely the spherical average technique and the power spectrum analysis, show that apart from small scales, there is good agreement between all three simulation results, Sem-Num lying within 15% and CPS+GS within 25% of the C^2-RAY results. The FoF method, which focuses on connectivity, shows that the Sem-Num and C^2-RAY results agree quite well, but CPS+GS shows fewer small and intermediate size H II regions, something which is also visible in Figure 2. This is partly due to the more inside-out nature of CPS+GS which means that a given mean ionized mass fraction corresponds to a smaller ionized volume fraction, but also because the ionized regions are more connected and more quickly merge to form larger ionized regions.

4.2 Cross-correlation

The cross-correlation between two different ionization fields A and B, defined as $\mathcal{R}_{xx}(k) = P_{AB}(k)/\sqrt{P_{AA}(k)P_{BB}(k)}$, estimates how spatially correlated the two fields are. We use $\mathcal{R}_{xx}(k)$ to quantify the strength of correlation between a semi-numerical simulation and C^2-RAY at different length scales. Figure 7 shows $\mathcal{R}_{xx}(k)$ estimated at four representative stages of EoR. From this figure it is evident that ionization maps from both of these semi-numerical schemes are highly correlated ($\mathcal{R}_{xx} \geq 0.95$) with that of C^2-RAY at sufficiently large length scales ($k \leq 0.1\,{\rm Mpc}^{-1}$), throughout almost all the stages of the EoR. Also, one of the main common features of these two cross-correlation coefficients is that they gradually decline at smaller length scales with the progress of reionization. However, this decline is faster for CPS+GS than for Sem-Num. In almost all stages of the EoR the cross-correlation between Sem-Num and C^2-RAY is $\mathcal{R}_{xx} \geq 0.75$ at $k \leq 1.0\,{\rm Mpc}^{-1}$, whereas at the same length scale range the cross-correlation between CPS+GS and C^2-RAY can become as low as $\mathcal{R}_{xx} \sim 0.1$. This cross-correlation analysis therefore further confirms the result that the morphology of the ionization fields obtained from Sem-Num resembles more that of C^2-RAY than CPS+GS. Our results are consistent with the findings of Zahn et al. (2011) in this regard.

We also estimate the cross-correlation between the ionization and the density field, defined as, $r_{\Delta x}(k) = P_{\Delta x}(k)/\sqrt{P_{xx}(k)P_{\Delta\Delta}(k)}$. This quantity tells us how the distribution of ionized regions in different simulation schemes are correlated with the underlying density field. Generally it is expected that overdense regions in the density field will ionize first as they are expected to host most of the ionizing sources. This is known as "inside-out" reionization. The cross-correlation coefficient $r_{\Delta x}(k)$ will directly quantify the strength of this "inside-out"-ness in different simulations. Figure 8 shows $r_{\Delta x}(k)$ for the three different simulations of reionization that we have discussed here. One general feature of $r_{\Delta x}(k)$ is that for all three simulations it is highest at the largest length scales and gradually declines

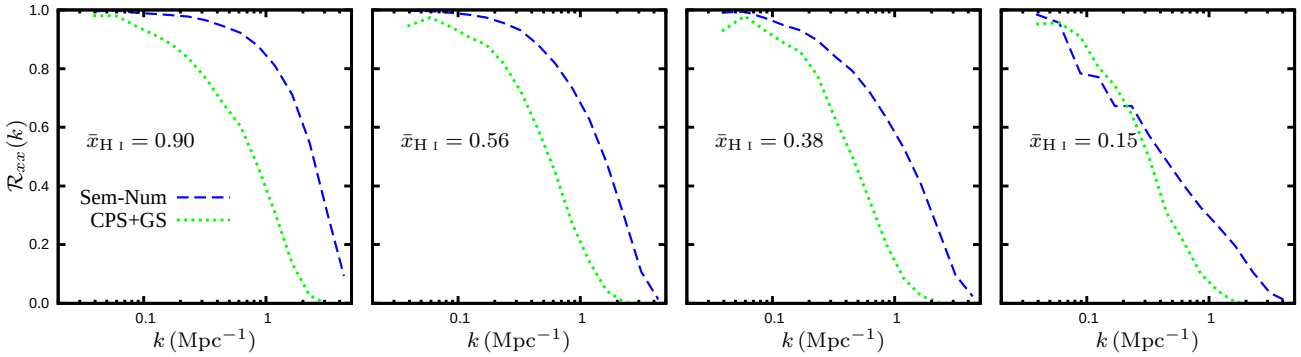

Figure 7. The cross-correlation $\mathcal{R}_{xx}(k)$ of the ionization maps of different semi-numerical schemes with the C^2-RAY simulation.

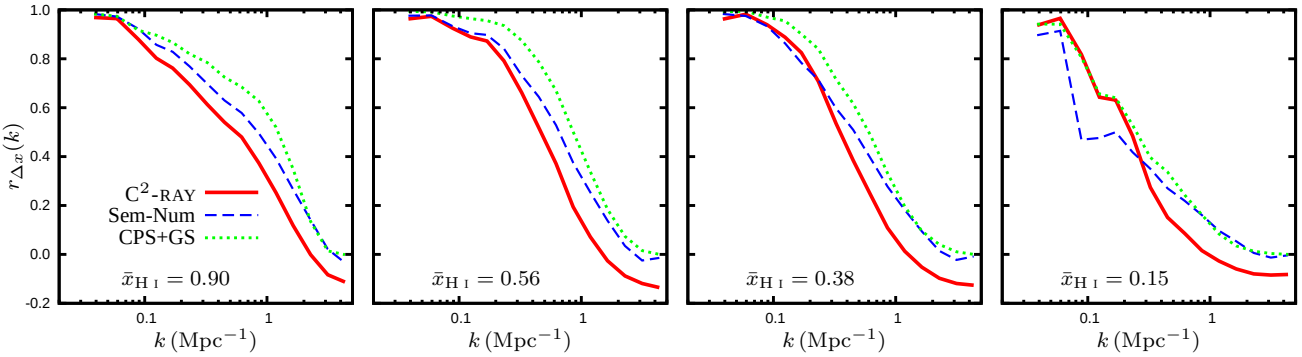

Figure 8. The cross correlation $r_{\Delta x}(k)$ between the ionization and the density field at four representative stages of reionization.

for smaller scales. Also, the strength of $r_{\Delta x}$ is higher in the early and the intermediate stages of EoR and smaller in the late stages of reionization. Among the two semi-numerical schemes, at large length scales ($k \leq 0.7\,{\rm Mpc}^{-1}$), Sem-Num follows C^2-RAY more closely than CPS+GS at almost all stages of the EoR.

The cross-correlation coefficient $r_{\Delta x}(k)$ is always highest for CPS+GS compared with the other two simulations, for all length scales and in all stages of the EoR. This shows that the CPS+GS is the most inside-out in nature among all three simulations discussed here. In other words, the ionization field of CPS+GS traces the matter distribution more closely than C^2-RAY and Sem-Num, which further supports our earlier observations. Similarly, we observe that C^2-RAY is the least inside-out among the three schemes. Sem-Num lies somewhere in between C^2-RAY and CPS+GS in terms of its inside-out nature. The cross-correlation coefficient $r_{\Delta x}$ for Sem-Num follows that of C^2-RAY very closely up to the length scales $k \leq 0.7\,{\rm Mpc}^{-1}$. For smaller length scales (*i.e.* higher k values) it follows the CPS+GS. The strong inside-out nature of the CPS+GS is in agreement with our earlier observations of the evolution of its history, bubble size distribution and the power spectrum of the ionization maps of this simulation. These results are also consistent with the findings of Zahn et al. (2011).

5 REDSHIFTED 21-CM SIGNAL

The major aim of the present and upcoming radio interferometric surveys of the EoR is to detect the redshifted H I 21-cm signal from this epoch. Once detected, reionization simulations can be used to interpret these observations. Hence it is very important to test different semi-numerical schemes for their ability to simulate this signal. The brightness temperature of the 21-cm H I radiation from EoR (when it can be assumed that the spin temperature is much higher than the CMBR temperature, $T_S \gg T_\gamma$) can be expressed as

$$\delta T_b(\mathbf{x}, z) = \overline{\delta T_b}(z)\,[1 + \delta_{\rho_{H\,I}}(\mathbf{x})]\ , \qquad (7)$$

where $\delta_{\rho_{H\,I}}(\mathbf{x})$ is the fluctuation in H I density at the point $\mathbf{x}$ and $\overline{\delta T_b}(z)$ is the mean brightness temperature at redshift z. We estimate the brightness temperature in real space from the ionization and the density fields of our simulations following eq. (7).

5.1 Redshift space distortions

Coherent inflows of matter (and gas) into overdense regions and outflows of matter (and gas) from underdense regions make the observed 21-cm signal anisotropic along the line of sight (LoS). This particular anisotropy in the signal is known as the redshift space distortions. We next explain how we have implemented the effects of the redshift space distortions on the brightness temperature maps generated from the simulations. One of the most accurate methods to include the effect of redshift space distortions is to include it at the level of each individual simulation particle. In this method one assumes that each particle from the N-body simulation contains an equal amount of hydrogen mass (M_H) before any reionization has actually taken place. The ionization map at each snapshot redshift provides us with a neutral fraction $x_{\rm H\,I}$ at each grid point of the simulation box. For each individual simulation particle one can then interpolate the neutral fraction from its eight nearest neigh-

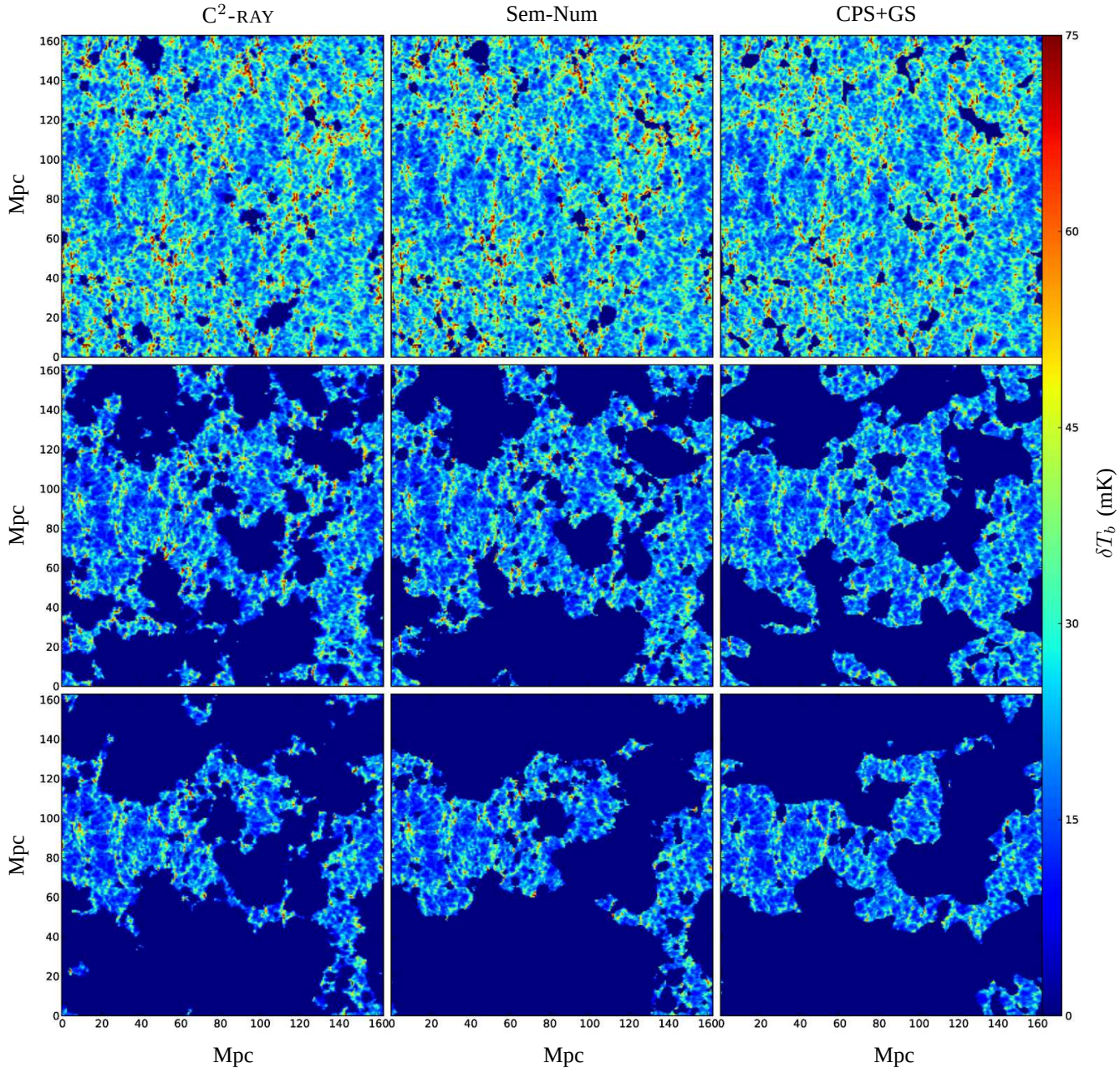

Figure 9. The redshift space 21-cm brightness temperature slices from three different simulations at three representative stages of reionization. The line of sight (LoS) is along the x-axis. From top to bottom three different rows correspond to $\bar{x}_{\rm H\,I} = 0.90$, 0.46 and 0.26 respectively. Thickness of each slice is 0.64 Mpc.

bouring grid points to determine the neutral fraction at that particle's position. This can be used to calculate the H I mass of the ith particle as $M^i_{H\,\rm I} = x^i_{\rm H\,I} M_H$. Next, one considers a distant observer located along the x axis and the x component of the peculiar velocity (v_x) of that particle is then used to determine its location in redshift space as

$$s = x + \frac{v_x}{aH(a)}\,, \tag{8}$$

where a and $H(a)$ are the scale factor and the Hubble parameter respectively. Finally, one interpolates the H I distribution from the particles to the grid and uses that to estimate the 21-cm signal in redshift space. This method of mapping the 21-cm signal from real to redshift space is similar to the PPM-RRM method of Mao et al. (2012) and also the method described by Majumdar, Bharadwaj & Choudhury (2013).

However, this method becomes computationally very expensive when one has to deal with a large number of particles (*e.g.* 3072^3 particles in our case). Therefore, instead of this particle based method we use the grid based method discussed in Jensen et al. (2013) to avoid this problem. In this method we divide each grid cell into n equal sub-cells along the LoS. If the brightness temperature of the original grid cell was $\delta T_b(\mathbf{x})$, then each sub-cell is assigned with a brightness temperature $\delta T_b(\mathbf{x})/n$. We then interpolate the velocity and density fields onto the sub-cells and move

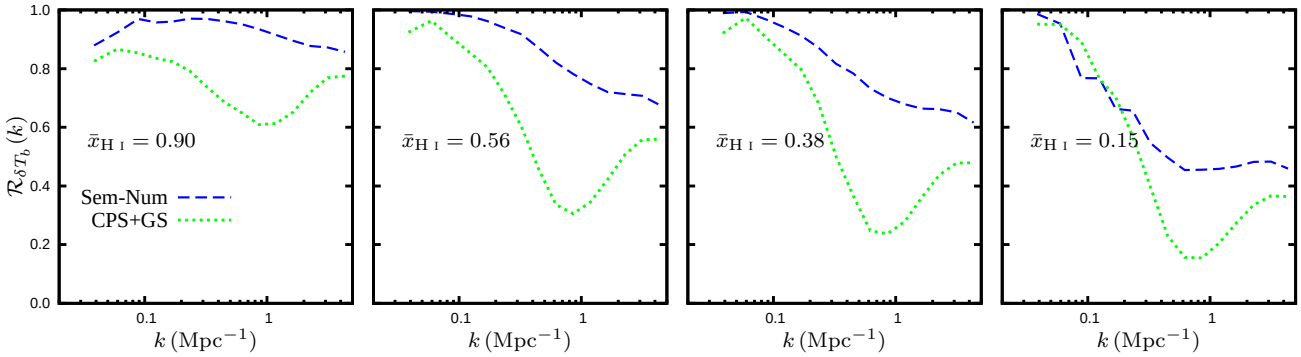

Figure 10. The cross-correlation $\mathcal{R}_{\delta T_b}(k)$ of the redshift space brightness temperature maps of two semi-numerical simulations with that of the C^2-RAY.

them according to eq. (8) and map the redshift space δT_b to the original grid again. For all the simulations described in this paper, we have used 50 sub-cells along the LoS for each original grid cell (of size 0.64 Mpc) to implement the redshift space distortions. This technique is somewhat similar to the MM-RRM method described in Mao et al. (2012). Figure 9 shows the brightness temperature maps in redshift space for the three different simulations discussed here at three different stages of the EoR.

5.2 Cross-correlation

Redshift space distortions will change the 21-cm signal along the LoS. It is thus important to compare the simulations discussed here in their ability to predict the redshifted 21-cm brightness temperature fluctuations as well as various other statistical measures of it in redshift space. We estimate the cross-correlation coefficient $\mathcal{R}_{\delta T_b}(k)$ between the redshift-space brightness temperature maps of the two semi-numerical simulations with that of C^2-RAY, to quantify how well the signal is reproduced by these semi-numerical schemes at different length scales. Figure 10 shows this cross-correlation coefficient $\mathcal{R}_{\delta T_b}(k)$ at different stages of the EoR. The overall characteristics of $\mathcal{R}_{\delta T_b}(k)$ shows that the semi-numerical schemes are more strongly correlated with C^2-RAY at the early stages of EoR than at the late stages and the correlation is higher at larger length scales and gradually declines towards smaller length scales.

We also observe that $\mathcal{R}_{\delta T_b}(k)$ for both of the semi-numerical schemes is much higher at all scales compared with $\mathcal{R}_{xx}(k)$ (the cross-correlation between ionization fields; see Figure 7). A possible reason for this is the following: The brightness temperature fluctuations δT_b are a combination of fluctuations in both the density field and the neutral fraction (see eq. [7]). All three simulations have the same density fluctuations (note that CPS+GS has a slightly diffused density field compared to the others) and they differ only in their ionization maps. In addition, for a completely neutral medium, redshift space distortions will effectively add some fluctuations to δT_b that are related to the density fluctuations. At the early stages of reionization the fluctuations in δT_b maps will thus be strongly dominated by density fluctuations rather than by fluctuations in the ionization field. This will make $\mathcal{R}_{\delta T_b}(k)$ higher than than $\mathcal{R}_{xx}(k)$. As reionization progresses, this dominance of density fluctuations will be gradually taken over by the fluctuations in the ionization maps. This will effectively reduce the cross-correlation $\mathcal{R}_{\delta T_b}$ at all scales.

Among the two semi-numerical simulations, Sem-Num provides a better reproduction of the signal than CPS+GS at almost all length scales and in all stages of reionization. For Sem-Num, $\mathcal{R}_{\delta T_b} \geq 0.7$ for $k \leq 1\,{\rm Mpc}^{-1}$ in almost all stages of reionization, whereas the same for CPS+GS is $\mathcal{R}_{\delta T_b} \geq 0.25$. At larger length scales ($k \geq 0.1\,{\rm Mpc}^{-1}$) the correlation is even stronger ($\mathcal{R}_{\delta T_b} \geq 0.95$) for Sem-Num whereas for CPS+GS, $\mathcal{R}_{\delta T_b} \geq 0.8$. The value of $\mathcal{R}_{\delta T_b}$ for Sem-Num never goes below 0.6 even at the smallest length scales until the end stages of the EoR ($\bar{x}_{\rm H\,I} \leq 0.15$). This cross-correlation with C^2-RAY establishes the fact that among the two semi-numerical schemes, Sem-Num provides a better representation of the observable signal than CPS+GS.

5.3 Comparison of Observable Quantities

The cross-correlation $\mathcal{R}_{\delta T_b}(k)$, presented in the previous section, shows that the semi-numerical schemes can provide a very good estimation for the redshifted 21-cm signal even up to considerably small length scales. However, neither the present (*e.g.* LOFAR, GMRT, 21CMA etc) nor the upcoming (*e.g.* SKA) radio interferometric arrays are able to image the signal with a precision comparable to the resolution of these simulations. LOFAR may be able to image the IGM during the EoR at relatively large length scales ($\geq 0.5^\circ$) (Zaroubi et al., 2012) or the individual H II regions around very bright sources (Geil et al., 2008; Majumdar, Bharadwaj & Choudhury, 2012; Datta et al., 2012), but the focus of the first generation of 21-cm EoR experiments will be on the statistical detection of the signal. In the following sections, we compare how well our simulations can predict various statistical measures of the 21-cm signal.

5.3.1 Variance of the 21-cm brightness temperature fluctuations

The variance of the 21-cm brightness temperature fluctuations holds the promise to be the statistical quantity through which the first detection of the EoR 21-cm signal may be possible. The variance essentially measures the power spectrum of the signal integrated over all observable wave numbers (or k modes). Once detected, in principle the variance can be parametrized to constrain the reionization redshift and its duration. It is anticipated that this might be achievable even with just 600 hr of observation using LOFAR (Patil et al., 2014).

Even for a very crude statistical measure of the EoR 21-cm signal, like the variance, the accurate implementation of the effect of peculiar velocities is important. We illustrate the effects of redshift space distortions on this observable quantity in the left panel

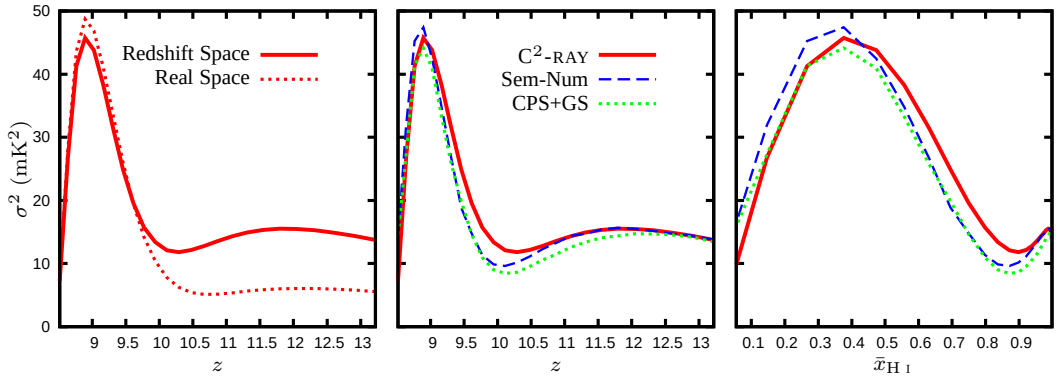

Figure 11. The evolution of the variance of the 21-cm brightness temperature. The left panel shows the evolution in real and redshift space with redshift as obtained from C^2-RAY. The central panel shows the evolution with z in redshift space for all three simulations. The right panel shows the same evolution with the neutral fraction $\bar{x}_{\rm H\,I}$. In all panels the variance has been estimated for a LOFAR-like baseline distribution and with a Gaussian approximation for the point spread function.

of Figure 11. This figure compares the evolution of the variance of the signal in real and redshift space, simulated using C^2-RAY. The variance shown here has been calculated for a LOFAR-like baseline distribution and with a Gaussian approximation for the point spread function of size $\sim 3.25'$ at 150 MHz in slices of thickness 38 kHz in frequency. Each volume contains 256 of such slices and we calculate the final variance of δT_b as the average over the variance of each of these slices, to reduce the uncertainties due to sampling errors.

We observe that the redshift space distortions change both the shape and the amplitude of the signal considerably during the early stages of reionization (*i.e.* for $z \geq 9.8$ and $\bar{x}_{\rm H\,I} \geq 0.8$ in this case). The amplitude of the variance in redshift space becomes significantly higher at this stage (≥ 2.5 times more with respect to the real space signal at $z \geq 10.6$ and $\bar{x}_{\rm H\,I} \geq 0.94$). The redshift space signal also shows a broad peak at $z \sim 11$ and $\bar{x}_{\rm H\,I} \sim 0.97$, whereas no such peak is visible in the real space signal. The redshift space variance has a very prominent dip at $z \sim 10.3$ and $\bar{x}_{\rm H\,I} \sim 0.9$, which is not visible in its real space counter part. This sharp decrement of the signal in the redshift space is probably a signature of the negative contribution from the cross-correlation between the density and the ionization field. According to the linear (Barkana & Loeb, 2005) as well as the quasi-linear (Mao et al., 2012) models of the redshift space distortions, this cross-correlation contributes more in the redshift space than in real space. All of these together increases the possibility of detection of the redshift space signal through the estimation of its variance. This broad peak and the sharp dip in the variance of the redshift space signal during the early stages of EoR has been ignored in the variance analysis of Patil et al. (2014). It is also worth mentioning that when the effect of peculiar velocities are incorporated in a perturbative fashion similar to Santos et al. (2010) and Mesinger et al. (2011) (as well as in Patil et al. 2014), it introduces an additional error of $\geq 20\%$ in the signal (Mao et al., 2012). Thus it is important to take into account the effect of the peculiar velocities accurately when parametrization of the observed variance is done on the basis of simulations. In the later stages of the EoR (*i.e.* $\bar{x}_{\rm H\,I} \leq 0.8$), the redshift space variance does not show any significant difference with its real space counterpart (deviation is $\leq 5\%$).

Next, we compare the predicted variance in redshift space from the three different simulations considered in this work. The central and the right panel of Figure 11 show this comparison through the evolution of the variance with redshift and $\bar{x}_{\rm H\,I}$, respectively. We observe that both of the semi-numerical simulations follow C^2-RAY very well. During the early phase of EoR (*i.e.* $z \geq 10.5$ and $\bar{x}_{\rm H\,I} \geq 0.92$), the Sem-Num follows the C^2-RAY more closely (deviation $\leq 8\%$) than the CPS+GS (deviation $\leq 20\%$). The deviation of the semi-numerical simulations from that of C^2-RAY is more prominent during the intermediate stages of reionization. This deviation from C^2-RAY peaks ($\sim 30\%$ for CPS+GS and $\sim 20\%$ for Sem-Num) near the point (around $z \sim 10.1$ and $\bar{x}_{\rm H\,I} \sim 0.87$) where the variance shows a sharp dip. We have found that among all three simulations CPS+GS is the most inside-out ($r_{\Delta x}$ in Figure 8) in nature. This implies that at this point the contribution of $r_{\Delta x}$ will be largest for CPS+GS, which will result in a much sharper dip in the variance predicted by this scheme. However, in the later stages of the EoR (*i.e.* $z \leq 9.6$ and $\bar{x}_{\rm H\,I} \leq 0.75$) the variance predicted by both of the semi-numerical simulations stay within $\sim 10\%$ of that of C^2-RAY. Thus it is the differences in the source models among the different semi-numerical schemes which causes the differences in the variance predicted by them.

5.3.2 *The redshift space 21-cm power spectrum and its angular multipole moments*

Redshift space distortions make the 21-cm signal from the EoR anisotropic. Thus the power spectrum will depend on both the wave number k and the quantity $\mu = \mathbf{k} \cdot \hat{\mathbf{n}}/k$, which is the cosine of the angle between the wave vector $\mathbf{k}$ and the unit vector $\hat{\mathbf{n}}$ along the LoS (Kaiser, 1987). It is convenient to decompose the anisotropy using Legendre polynomials $\mathcal{P}_l(\mu)$ (Hamilton, 1992; Cole et al., 1995) as

$$P^s(k,\mu) = \sum_{l\,\rm even} \mathcal{P}_l(\mu) P_l^s(k)\,, \qquad (9)$$

where $P_l^s(k)$ are the different angular multipoles of $P^s(k,\mu)$. This decomposition of the anisotropy is a representation in an orthonormal basis. Thus different angular multipole moments in this representation are orthogonal to each other (Majumdar, Bharadwaj & Choudhury, 2013). The anisotropic power spectrum can also be decomposed in different coefficients of the powers of μ (Mao et al., 2012). However these coefficients will not be completely independent of each other and the correlation between them (or the leak-

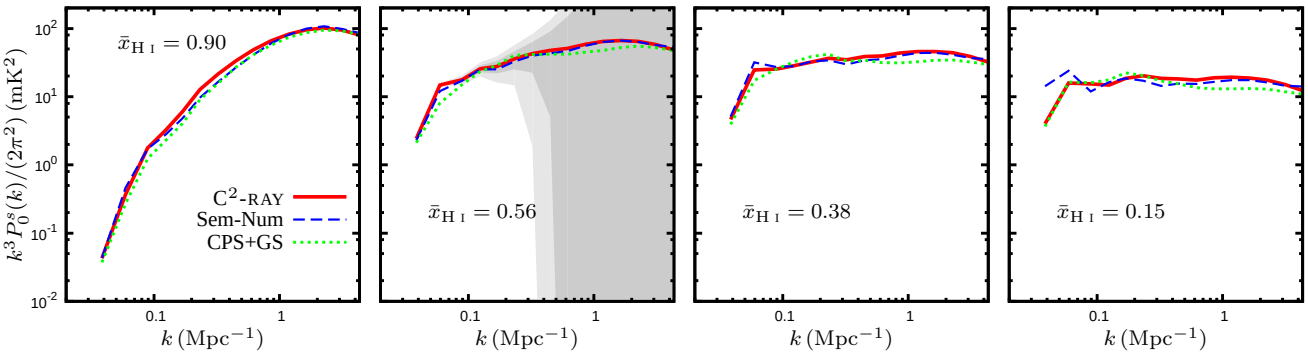

Figure 12. The spherically averaged power spectrum of the redshift space 21-cm signal. The shaded regions in light and dark gray represent the uncertainty due LOFAR-like system noise at 150 MHz for 1000 and 2000 hr of observation respectively.

age of power from one component to the other) sometimes may give rise to slightly wrong interpretations (Jensen et al., 2013). On the basis of these angular multipole moments of the redshift space power spectrum we compare our semi-numerical schemes with C^2-RAY. As far as we know, such a comparison has not been made before.

We Fourier transform the brightness temperature data cubes obtained from different simulations and estimate the angular multipoles P_l^s of the redshifted 21-cm power spectrum from the Fourier transformed data following the equation

$$P_l^s(k) = \frac{(2l+1)}{4\pi} \int \mathcal{P}_l(\mu)\, P^s(k)\, d\Omega\,, \tag{10}$$

where $P^s(k)$ is the 21-cm power spectrum in redshift space. The integral is done over the entire solid angle to take into account all possible orientations of the $\mathbf{k}$ vector with the LoS direction $\hat{\mathbf{n}}$. Each angular multipole is estimated at 15 logarithmically spaced k bins in the range $0.038 \leq k \leq 4.90\,{\rm Mpc}^{-1}$. It is obvious from eq. (9) and (10) that the $0^{\rm th}$ angular moment or the monopole (P_0^s) will be essentially the spherically averaged 3D power spectrum in redshift space.

To better understand and interpret our results, we have considered two models for the redshift space power spectrum. The first of these uses the linear approximations described in Barkana & Loeb (2005) to express the redshift space power spectrum as:

$$P^s(k,\mu) = \overline{\delta T_b}^2(z)\left[P_{x_{\rm H\,I}x_{\rm H\,I}}(k) + 2(1+\mu^2)P_{\Delta x_{\rm H\,I}}(k) + (1+\mu^2)^2 P_{\Delta\Delta}(k)\right] \tag{11}$$

where $\Delta_{x_{\rm H\,I}}$ and Δ are the Fourier transform of the neutral fraction and the density fluctuations and $P_{x_{\rm H\,I}x_{\rm H\,I}}$, $P_{\Delta\Delta}$ are the power spectra of these two quantities respectively, and $P_{\Delta x_{\rm H\,I}}$ is the cross power spectrum between Δ and $\Delta_{x_{\rm H\,I}}$. In this model only the first three even angular moments of the redshift space power spectrum have non-zero values

$$P_0^s = \overline{\delta T_b}^2(z)\left(\frac{28}{15}P_{\Delta\Delta} + \frac{8}{3}P_{\Delta x_{\rm H\,I}} + P_{x_{\rm H\,I}x_{\rm H\,I}}\right), \tag{12}$$

$$P_2^s = \overline{\delta T_b}^2(z)\left(\frac{40}{21}P_{\Delta\Delta} + \frac{4}{3}P_{\Delta x_{\rm H\,I}}\right), \tag{13}$$

$$P_4^s = \overline{\delta T_b}^2(z)\left(\frac{8}{35}\right)P_{\Delta\Delta}\,. \tag{14}$$

In the quasi-linear model of Mao et al. (2012), the same redshift space power spectrum can be expressed as

$$P^s(k,\mu) = \overline{\delta T_b}^2(z)\left[P_{\rho_{H\,\rm I}\rho_{H\,\rm I}}(k) + 2\mu^2 P_{\rho_{H\,\rm I}\rho_H}(k) + \mu^4 P_{\rho_H\rho_H}(k)\right] \tag{15}$$

where $\Delta_{\rho_{H\,\rm I}}$ and Δ_{ρ_H} are the Fourier transform of the neutral and the total hydrogen density fluctuations and $P_{\rho_{H\,\rm I}\rho_{H\,\rm I}}$, $P_{\rho_H\rho_H}$ are the power spectra of $\Delta_{\rho_{H\,\rm I}}$ and Δ_{ρ_H} respectively, and $P_{\rho_{H\,\rm I}\rho_H}$ is the cross power spectrum between $\Delta_{\rho_{H\,\rm I}}$ and Δ_{ρ_H}. Also in this case only the first three even angular multipole moments will have non-zero values

$$P_0^s = \overline{\delta T_b}^2(z)\left(\frac{1}{5}P_{\rho_H\rho_H} + \frac{2}{3}P_{\rho_{H\,\rm I}\rho_H} + P_{\rho_{H\,\rm I}\rho_{H\,\rm I}}\right), \tag{16}$$

$$P_2^s = \overline{\delta T_b}^2(z)\left(\frac{4}{7}P_{\rho_H\rho_H} + \frac{4}{3}P_{\rho_{H\,\rm I}\rho_H}\right), \tag{17}$$

$$P_4^s = \overline{\delta T_b}^2(z)\left(\frac{8}{35}\right)P_{\rho_H\rho_H}\,. \tag{18}$$

All the simulations discussed here work with the underlying assumption that the baryons follow the dark matter distribution. This essentially implies that the density fluctuations Δ and the total hydrogen (ionized + neutral) density fluctuations Δ_{ρ_H} are essentially the same quantity. Thus their power spectra are also the same (*i.e.* $P_{\Delta\Delta} = P_{\rho_H\rho_H}$). This means that according to both of these models the $4^{\rm th}$ moment (or the hexadecapole P_4^s) measures the density power spectrum.

We first focus on the monopole moment (P_0^s) of the 21-cm redshift space power spectrum (*i.e.* the spherically averaged power spectrum), which measures the strength of the signal at different length scales averaged over all angles. Figure 12 shows the monopole moment of the power spectrum for different simulations at four representative stages of EoR. We observe that the differences between the predictions for P_0^s from C^2-RAY and the semi-numerical schemes is relatively small for almost all stages of the EoR. In case of Sem-Num the predictions deviates from C^2-RAY by $\leq 10\%$ for most of the length scales. This difference goes up to 20% at most in some stages. In case of the CPS+GS the P_0^s deviates from that of the C^2-RAY by $\leq 20\%$ for most length scales at almost all stages and the difference can reach 40% at certain stages of the EoR. Overall, CPS+GS tends to underestimate the power in some large and most of the small length scales. This is probably a signature of the stronger correlation between the density and the ionization field (see Figure 8) in case of CPS+GS. According to

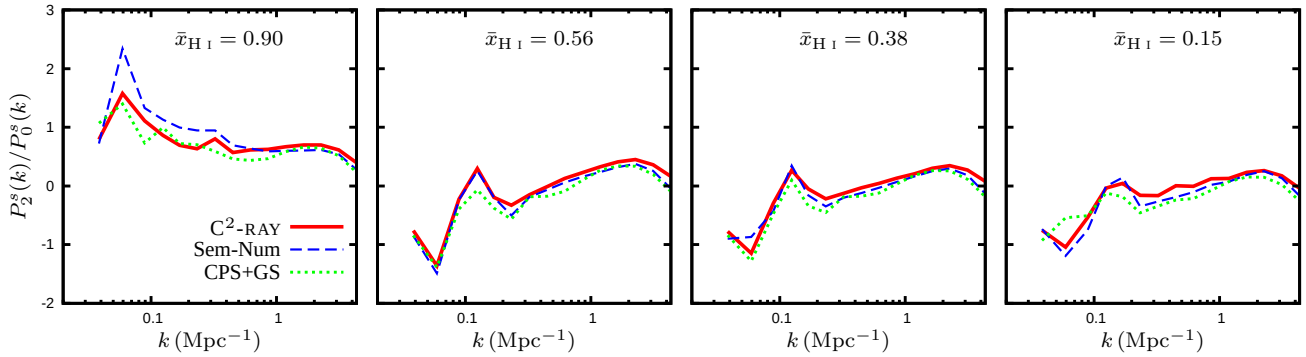

Figure 13. The ratio $P_2^s(k)/P_0^s(k)$ at four representative stages of the EoR.

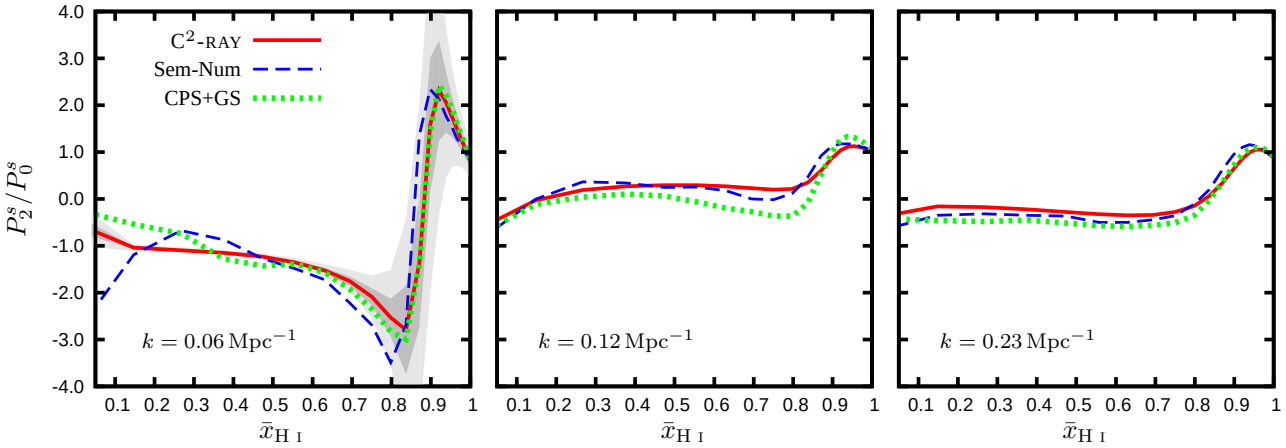

Figure 14. The evolution of the ratio P_2^s/P_0^s with $\bar{x}_{\rm H\,I}$ at three representative k values. The shaded regions in light and dark gray represent uncertainty due to the system noise for 2000 and 5000 hr of observation using a LOFAR like instrument at 150 MHz.

both models of redshift space distortions discussed above (eq. [12] and [16]) the cross-correlation power spectrum between the density and the neutral fraction or the neutral density field contributes negatively to P_0^s. Since the ionization map produced using the CPS+GS is more strongly correlated with density field than the other two simulations, this makes the amplitude of the P_0^s lower in case of CPS+GS.

The shaded regions in the Figure 12 (in the 2nd panel from left) show the uncertainties in the measurements of the $0^{\rm th}$ moment due to the system noise for a LOFAR like instrument at 150 MHz (McQuinn et al., 2006; Datta et al., 2012; Jensen et al., 2013). It is evident from this figure that even after 1000 or 2000 hr of observation the signal will still possibly be dominated by the noise for k modes $\geq 0.35\,{\rm Mpc}^{-1}$ or $\geq 0.50\,{\rm Mpc}^{-1}$, respectively. Thus it would be of interest to see how well the semi-numerical methods perform in predicting the signal for k values smaller than these limits. At these large length scales, the P_0^s estimated from both of the semi-numerical simulations show significantly less difference from the same predicted by C^2-RAY. This difference from C^2-RAY is less than 25% for the CPS+GS and less than 15% for the Sem-Num for k values below these upper limits.

The $2^{\rm nd}$ moment P_2^s (*i.e.* the quadrupole moment) essentially measures the anisotropy due to the peculiar velocities in the signal. The presence of a measureable non-zero quadrupole moment itself will be evidence of redshift space distortions. The ratio between the quadrupole and the monopole moments $[P_2^s(k)/P_0^s(k)]$ of the 21-cm power spectrum can be used to quantify the strength as well as the nature of the redshift space distortions present in the observed signal. In principle it is possible to constrain the reionization model if the nature and the evolution of this ratio during the EoR can be probed with sufficient accuracy (Majumdar, Bharadwaj & Choudhury, 2013). Figure 13 shows the $P_2^s(k)/P_0^s(k)$ estimated from the three different simulations at four representative stages of EoR. One can easily figure out the prominent general features of this observable quantity from this figure. At the early stages of reionzation ($\bar{x}_{\rm H\,I} \geq 0.9$) this ratio is positive at all length scales. Once this phase is over ($\bar{x}_{\rm H\,I} < 0.9$), it becomes negative at larger length scales ($\leq 0.50\,{\rm Mpc}^{-1}$), due to the strong contribution from the cross-correlation term (see eq. [13] and [17]). This ratio also developes a positive slope at this stage of EoR, which gradually reduces as reionization progresses. It is clear from Figure 13 that most of these important general features observed in C^2-RAY simulation are reproduced well by both of the semi-numerical simulations discussed here. We further compare the semi-numerical simulations with C^2-RAY in the length scale range ($k \leq 0.50\,{\rm Mpc}^{-1}$), where it is possible to detect P_0^s. At the early stages of EoR for this length scale range, CPS+GS produces a better match with that of the C^2-RAY (deviation is $\leq 15\%$), than Sem-Num (deviation is $\leq 25\%$ and at $k \leq 0.05\,{\rm Mpc}^{-1}$ it may go above 50%). However, after the initial stages of EoR ($\bar{x}_{\rm H\,I} \leq 0.9$), the predictions from

Sem-Num (deviation is $\leq 20\%$) are better matched with C^2-RAY, than CPS+GS (deviation is $\leq 30\%$). The major reason for this difference in case of CPS+GS is possibly that the cross-correlation between the density and the ionization field is much stronger in this case than in Sem-Num or C^2-RAY.

To study this ratio in further detail, we show its evolution in Figure 14 at three representative length scales ($k = 0.06,\ 0.12 \,\mathrm{and}\, 0.23\,\mathrm{Mpc}^{-1}$). For all three simulations the evolution of this ratio can be characterised in general by a sharp positive peak and a negative dip at the early phase of EoR ($\bar{x}_{\mathrm{H\,I}} \sim 0.9$). Once this early phase is over, P_2^s/P_0^s remains negative for the remaining period of EoR. However, the amplitude of this ratio and the sharpness of its transition from positive to negative is largest at the largest length scales ($k = 0.06\,\mathrm{Mpc}^{-1}$). At intermediate and smaller length scales ($k = 0.12 \,\mathrm{and}\, 0.23\,\mathrm{Mpc}^{-1}$ respectively), its amplitude reduces significantly and the sharp transition region becomes more and more flattened.

These features are consistent with the earlier observation of this quantity using a simulation equivalent to Sem-Num by Majumdar, Bharadwaj & Choudhury (2013). This sharp peak and dip can be explained by the contribution from the cross power spectrum term (between density and neutral fraction or neutral density) in eq. (13) or (17). This contribution will be at a maximum in case of a strictly "inside-out" model. The location and the amplitude of this feature essentially measures the strength of "inside-out"-ness of the simulation. Thus this transition from positive to negative value can be used as a definite indicator for the onset of reionization. We observe that all three simulations discussed here produce these features at the same location (at $\bar{x}_{\mathrm{H\,I}} \sim 0.8 - 0.9$) and with almost the same amplitude (with a maximum of $\sim 10\%$ deviation from each other). Thus one can safely say that the semi-numerical schemes are robust enough to reproduce the main observable features introduced by redshift space distortions.

The shaded regions in light and dark gray in the left most panel of Figure 14 show the uncertainty in the measurement of this ratio due to the system noise after 2000 and 5000 hr of observation using a LOFAR like instrument. We observe that the predictions for this ratio by both of the semi-numerical simulations fall well within the noise uncertainty of LOFAR. At the largest scales ($k = 0.06\,\mathrm{Mpc}^{-1}$) CPS+GS produces a slightly better match with C^2-RAY (deviation is $\leq 10\%$ for $0.2 \leq \bar{x}_{\mathrm{H\,I}} \leq 1.0$) than Sem-Num (deviation is $\leq 15\%$). Note that at these length scales uncertainties due to sample variance are expected to be higher than at smaller length scales. However, at intermediate and smaller length scales predictions by Sem-Num are closer to C^2-RAY than those from CPS+GS are. Note that at smaller length scales the contribution of noise is expected to be higher but the contribution from sample variance is expected to be lower.

The next statistical quantity of interest with an observing potential is the hexadecapole moment (P_4^s). If detected, this quantity will essentially probe the underlying matter density fluctuations. Similar to the quadrupole moment this can be described through the ratio $P_4^s(k)/P_0^s(k)$. For a completely neutral IGM both the linear and quasi-linear model predict a much smaller value for this ratio (≈ 0.12) than for $P_2^s(k)/P_0^s(k)$ (≈ 1.02). This will make its detection much more difficult and a longer integration time or/and higher sensitivity of the instrument would be required. We find that at the larger length scales relevant for the present day EoR experiments, the three simulations considered here agree well (differences $\leq 10\%$) in terms of this ratio. However these results are dominated by sample variance as they fluctuate considerably and even produce negative values. Therefore we do not include this quantity in our comparison analysis.

Although not relevant for the comparison presented here, we would like to note that, all the simulations discussed here, have not taken into account the effect of spin temperature fluctuations. The assumption of $T_S \gg T_\gamma$ may break down in a situation when 21-cm is observed in absorption against the CMBR (Mao et al., 2012). This may happen at the very early stages of the EoR, when the first astrophysical sources are formed and they start coupling the spin temperature with the kinetic temperature of the IGM by Lyman-α pumping. Further, this period of $T_S < T_\gamma$ can be shortend or extended due to the effect of X-ray heating in the early universe (Mesinger et al., 2013). These studies further show that the fluctuations in the spin temperature can boost the 21-cm powerspectrum by more than an order of magnitude during this early phase of reionization. The spin temperature fluctuations may also impact the signal at ten percent level even when $T_S > T_\gamma$ well into reionization. The fluctuations in the spin temperature due to all these effects may introduce an additional fluctuation in the 21-cm brightness temperature δT_b, which may further complicate the interpretation of the redshift space 21-cm signal from this era (Mao et al., 2012; Ghara et al., 2014). We plan to address these issues in a future work.

6 SUMMARY AND CONCLUSIONS

A common notion about semi-numerical methods is that they are not reliable for recreating the ionization history, since they do not chronologically follow the state of ionization at individual grid cells. Our comparison between one numerical simulation (C^2-RAY) and two semi-numerical simulations (Sem-Num and CPS+GS) does not support this idea. We find that between Sem-Num and C^2-RAY the average reionization history in terms of $\langle x_{\mathrm{H\,I}} \rangle_v / \langle x_{\mathrm{H\,I}} \rangle_m$ differs by a maximum of $\sim 5\%$, whereas the same difference between CPS+GS and C^2-RAY can be $\sim 10\%$ at the late stages of EoR. We examine the reconstruction of the reionization history further by estimating the bias $[b_{z\Delta}(k)]$ and cross-correlation $[r_{z\Delta}(k)]$ between the redshift of reionization and density fluctuations at different length scales. We find that $b_{z\Delta}(k)$ for Sem-Num and CPS+GS is in excellent agreement ($\leq 5\%$ difference) with that of C^2-RAY for a wide range of length scales ($k \leq 1.0\,\mathrm{Mpc}^{-1}$). However, the cross-correlation $r_{z\Delta}(k)$ for CPS+GS is higher than C^2-RAY by $\sim 60\%$ (for $k \leq 0.8\,\mathrm{Mpc}^{-1}$) and the same for Sem-Num is higher than C^2-RAY by $\sim 25\%$.

We have quantified and compared the morphology of the ionization maps from semi-numerical simulations with that of C^2-RAY using the bubble size distribution, the power spectrum and the cross-correlation. The bubble size distribution as well as the evolution of $\langle x_{\mathrm{H\,I}} \rangle_v / \langle x_{\mathrm{H\,I}} \rangle_m$ reveals that the total volume ionized in CPS+GS at any stage of the EoR is smaller than in both Sem-Num and C^2-RAY. Specifically, CPS+GS produces fewer small bubbles. The spherically-averaged power spectrum $P_{xx}(k)$, however, does not show a large difference between the semi-numerical models and C^2-RAY. The difference between C^2-RAY and Sem-Num is within $\sim 15\%$ and the same with CPS+GS is within $\sim 25\%$ for a wide range of length scales ($0.04 \leq k \leq 2.0\,\mathrm{Mpc}^{-1}$) during most of the EoR ($0.2 \leq \bar{x}_{\mathrm{H\,I}} \leq 0.85$). The cross-correlation between the ionization maps of the semi-numerical simulations and that of C^2-RAY shows that Sem-Num is strongly correlated with C^2-RAY ($R_{xx} \geq 0.8$) at large and intermediate length scales ($k \leq 0.7\,\mathrm{Mpc}^{-1}$; relevant for 21-cm observations), whereas the same for CPS+GS is

relatively poor ($R_{xx} \geq 0.3$). Also, at smaller length scales the cross-correlation falls more rapidly for CPS+GS than for Sem-Num. The cross-correlation between the density fields and ionization maps ($r_{\Delta x}$) shows that the ionization maps in CPS+GS follows the cosmic web more strongly at all length scales than the other two schemes. The difference in morphology between the semi-numerical simulations and C^2-RAY, especially at small scales, is likely due to the former's assumption of uniform recombination.

From our analysis of the reionization history, bias [$b_{z\Delta}(k)$], cross-correlation [$r_{z\Delta}(k)$], bubble size distribution, power spectrum [$P_{xx}(k)$] and cross-correlation [$R_{xx}(k)$ and $r_{\Delta x}(k)$], we can safely conclude that the reionization history and the morphology of the ionization maps of C^2-RAY are reproduced with higher accuracy by Sem-Num than by CPS+GS. These differences are due to the fact that CPS+GS produces a higher degree of "inside-out" reionization, i.e. reionization is more biased to denser regions.

The main algorithmic difference between the two semi-numerical schemes lies in their assumptions regarding the modelling of reionization sources. Sem-Num takes into account the reionization sources in a manner very similar to C^2-RAY. It considers the halos identified from the N-body particle distribution as the hosts of ionizing sources (eq. [3]), whereas CPS+GS does not incorporate halo masses and locations in its source model, but rather estimates the collapsed fraction from the density field directly. This causes the reionization to be more "inside-out" in nature for CPS+GS. It also makes it necessary to smooth the N-body density field in CPS+GS (e.g. by using a Gaussian filter); otherwise both the morphology of ionized regions and the reionization history become markedly different from C^2-RAY.

None of the above quantities are actual observables. The most direct observable of the reionization process is the redshifted 21-cm signal from neutral hydrogen. When comparing the results for this quantity between the three simulations, we observe that Sem-Num stays highly correlated ($\mathcal{R}_{\delta T_b} \geq 0.8$) with C^2-RAY at length scales relevant for present and future experiments such as LOFAR, MWA, GMRT etc. ($k \leq 0.5\,\mathrm{Mpc}^{-1}$) during almost the entire span of the EoR ($0.2 \leq \bar{x}_{\mathrm{H\,I}} \leq 1.0$). However, the same correlation between CPS+GS and C^2-RAY is much worse ($\mathcal{R}_{\delta T_b} \geq 0.4$).

The first observations of the redshifted 21-cm signal will concentrate on simpler statistical measures, such as the variance of the signal. We observe that the predictions for the variance from both the semi-numerical schemes are in well agreement with that of the C^2-RAY. The deviation from C^2-RAY at maximum is approximately 20% and approximately 30% for Sem-Num and CPS+GS, respectively. These differences fall well inside the measurement errors of a LOFAR-like experiment (Patil et al., 2014).

As an aside we find that a correct implementation of redshift space distortions is important for the 21-cm signal, even when considering the simplest statistic, namely the variance. The shape and amplitude of the variance differ considerably between real and redshift space, especially during the early stages of reionization. Thus it is essential to incorporate the redshift space distortions accurately using the actual peculiar velocity fields when trying to constrain the reionization parameters using the evolution of the redshifted 21-cm signal from EoR.

We further considered the different angular multipole moments of the redshifted 21-cm power spectrum. Predictions for the monopole moment [$P_0^s(k)$] or the spherically averaged power spectrum from semi-numerical simulations show good agreement with the results from C^2-RAY. The $P_0^s(k)$ estimated from Sem-Num and CPS+GS deviates by $\leq 15\%$ and $\leq 25\%$ respectively from C^2-RAY at length scales $k \leq 0.5\,\mathrm{Mpc}^{-1}$. The power spectrum at these length scales will possibly become detectable after more than 1000 hours of LOFAR observations.

The strength and the nature of the redshift space distortions present in the 21-cm signal can be quantified by the ratio between the quadrupole and the monopole moments of the redshift space power spectrum [$P_2^s(k)/P_0^s(k)$] (Majumdar, Bharadwaj & Choudhury, 2013). The properties and evolution of this ratio, in principle, can also help in characterising/constraining the nature of reionization and its sources. We observe that all three simulations discussed here capture and represent the major characteristic features of an "inside-out" reionization through the ratio $P_2^s(k)/P_0^s(k)$. We find that Sem-Num performs slightly better (deviation from C^2-RAY is $\leq 15\%$) than CPS+GS (deviation from C^2-RAY is $\leq 20\%$) in terms of the prediction for this ratio at length scales ($k \leq 0.23\,\mathrm{Mpc}^{-1}$) that will be detectable after more than 2000 hours of LOFAR observations. However, both of the semi-numerical results stays within the noise uncertainties that will be present in such observations.

In conclusion, we can say that both semi-numerical models discussed here perform reasonably well in predicting the observables of the 21-cm signal from EoR at length scales detectable with the present and future experiments, provided that the effect of redshift space distortions has been implemented in them with an acceptable accuracy. We also observe that the predictions from Sem-Num are slightly more similar to C^2-RAY (by $\sim 10\%$) than CPS+GS for most of the observables. However, the predictions for the reionization history and the morphology of the ionization maps are significantly closer to the benchmark (by $\sim 25-50\%$) in Sem-Num than CPS+GS mainly due to the differences in their source model. As the predictions for the 21-cm signal together with the reionization history would be required for the parameter estimation from the observational data, it would be better to use a semi-numerical scheme which can predict both with an acceptable accuracy. We find that among the two semi-numerical simulations discussed here Sem-Num satisfies this criterion very well, as it incorporates a source model very similar to C^2-RAY. However, we should note that any halo based simulation technique (radiative transfer or semi-numerical) is restricted by its particle mass resolution in terms of the dynamic range that it can explore. On the other hand simulation techniques based on the conditional Press-Schechter approach is not restricted by its mass resolution, as the limit on minimum halo mass in the source model ($\sigma^2(R_{\mathrm{min}})$ in the denominator of eq. [5]) is introduced analytically. This kind of prescription thus can include atomically or molecularly cooling halos through this analytical approach.

As we explained in the introduction, we on purpose chose a somewhat simplified case for our comparison. Here we would like to review briefly some of the effects which we do not consider. The first one is the effect of radiative feedback on the star formation in low mass halos. Because of the shallowness of their gravitational potential, halos of masses less than $\sim 10^9 M_\odot$ will stop accreting gas from the IGM once it has been ionized and heated to temperatures of $\sim 10^4$ K. This will most likely affect their star formation efficiency, although the details remain unclear (Couchman & Rees, 1986; Rees, 1986; Efstathiou, 1992; Thoul & Weinberg, 1995, 1996; Gnedin, 2000; Kitayama et al., 2000; Dijkstra et al., 2004; Hoeft et al., 2006; Okamoto et al., 2008). Since this type of feedback depends on the distribution of the ionized regions, including it could increase the differences between numerical and semi-numerical results. Furthermore, as this effect depends on the local history of reionization, including it in numerical simulations is rather straightforward but including it semi-numerical simulations is more complicated. The reason for this is that in the semi-

numerical approach the photon production in a given region is determined by the collapsed mass in the chosen mass range of halos rather than on the actual history of halos in that region. Sobacchi & Mesinger (2013) recently proposed a method to include this feedback effect in a semi-numerical simulation. It would be useful to compare the results of this approach to a full numerical simulation with a radiative feedback recipe.

The second effect we did not consider is the impact of unresolved density fluctuations. In fully ionized regions these will boost the recombination rate and the densest structures will even be self-shielding for ionizing photons and remain (partly) neutral, blocking the path of ionizing photons. The effect of these will be to increase the number of photons needed to reionize the Universe, as a larger fraction will have to be used for balancing recombinations. The presence of these structures will also limit the mean free path of ionizing photons. So-called Lyman Limit Systems are often mentioned in this context. These features in quasar spectra represent small scale structures which are optically thick to ionizing photons, although they do not need to be fully self-shielding. These inhomogeneous recombinations will limit the growth of ionized regions and therefore reduce the fluctuations in the 21-cm signal on large scales (e.g. see Sobacchi & Mesinger 2014, Shukla et al., in preparation). This will possibly have a significant effect in shaping the spherically averaged power spectrum of the 21-cm signal from this epoch.

Simulations which do not resolve the full range of density fluctuations, including the self-shielded systems will thus reionize too quickly and, due to the long mean free paths for ionizing photons, produce local photo-ionization rates which are too high. As mentioned in Section 2.2 for numerical simulations it is possible to introduce a clumping factor to correct for this lack of resolution although doing this completely self-consistently is not trivial. The semi-numerical methods can correct for the enhanced recombination inside self-shielded neutral regions through sub-grid modelling (Choudhury et al., 2009; Sobacchi & Mesinger, 2014). However, since these approaches are not fully equivalent, we have chosen not to include any subgrid corrections for density fluctuations here. As for the radiative feedback, it would be good to compare the different implementations for the effects of density fluctuations between numerical and semi-numerical methods. However, we consider this to be beyond the scope of this paper. We postpone such a comparison to future work.

Lastly, when calculating the 21-cm signal from our simulations, we have not taken into account the effect of spin temperature fluctuations. The spin temperature fluctuations due to the Lyman-α pumping and also due to the heating by X-ray sources can affect the 21-cm brightness temperature fluctuations significantly during the early stages of EoR (Mesinger et al., 2013). These additional fluctuations in the 21-cm brightness temperature may further complicate the interpretation of the redshift space 21-cm signal from this era (Mao et al., 2012; Ghara et al., 2014). We plan to address this issue in a future work.

ACKNOWLEDGMENTS

The authors would like to thank Ilian T. Iliev for his constructive comments on the initial version of the manuscript. SM would like to thank Andrei Mesinger for the useful discussions during a workshop titled “Lyman-alpha as an astrophysical tool” organized by NORDITA and the Department of Astronomy of Stockholm University in September 2013. KKD thanks the Department of Science & Technology (DST), India for the research grant SR/FTP/PS-119/2012 under the Fast Track Scheme for Young Scientist.

References

Alvarez, M. A., Shapiro, P. R., Ahn, K., & Iliev, I. T. 2006, ApJL, 644, L101
Alvarez, M. A., Busha, M., Abel, T., & Wechsler, R. H. 2009, ApJL, 703, L167
Barkana, R., & Loeb, A. 2004, ApJ, 609, 474
Barkana, R., & Loeb, A. 2005, ApJL, 624, L65
Barkana, R., & Loeb, A. 2008, MNRAS, 384, 1069
Battaglia, N., Trac, H., Cen, R., & Loeb, A. 2013, ApJ, 776, 81
Becker, R. H., Fan, X., White, R. L., et al. 2001, AJ, 122, 2850
Bharadwaj, S., Nath, B. B., & Sethi, S. K. 2001, Journal of Astrophysics and Astronomy, 22, 21
Bharadwaj, S., & Ali, S. S. 2004, MNRAS, 352, 142
Bond, J. R., Cole, S., Efstathiou, G., & Kaiser, N. 1991, ApJ, 379, 440
Bowman, J. D., Cairns, I., Kaplan, D. L., et al. 2013, Pub. Astro. Soc. Australia, 30, 31
Choudhury, T. R., Haehnelt, M. G., & Regan, J. 2009, MNRAS, 394, 960
Ciardi, B., Ferrara, A., Marri, S., & Raimondo, G. 2001, MNRAS, 324, 381
Cole, S., Fisher, K. B., & Weinberg, D. H. 1995, MNRAS, 275, 515
Couchman, H. M. P., & Rees, M. J. 1986, MNRAS, 221, 53
Datta, K. K., Friedrich, M. M., Mellema, G., Iliev, I. T., & Shapiro, P. R. 2012, MNRAS, 424, 762
Dijkstra, M., Haiman, Z., Rees, M. J., & Weinberg, D. H. 2004, ApJ, 601, 666
Efstathiou, G. 1992, MNRAS, 256, 43P
Fan, X., Strauss, M. A., Schneider, D. P., et al. 2003, AJ, 125, 1649
Friedrich, M. M., Mellema, G., Alvarez, M. A., Shapiro, P. R., & Iliev, I. T. 2011, MNRAS, 413, 1353
Furlanetto, S. R., Zaldarriaga, M. & Hernquist, L. 2004, ApJ, 613, 1
Geil, P. M., & Wyithe, J. S. B. 2008, MNRAS, 386, 1683
Geil, P. M., Wyithe, J. S. B., Petrovic, N., & Oh, S. P. 2008, MNRAS, 390, 1496
Ghara, R., Choudhury, T. R., & Datta, K. K. 2014, arXiv:1406.4157
Gnedin, N. Y. 2000, ApJ, 535, 530
Gnedin, N. Y. 2000, ApJ, 542, 535
Goto, T., Utsumi, Y., Hattori, T., Miyazaki, S., & Yamauchi, C. 2011, MNRAS, 415, L1
Hamilton, A. J. S. 1992, ApJL, 385, L5
Harnois-Déraps, J., Pen, U.-L., Iliev, I. T., et al. 2013, MNRAS, 436, 540
Hoeft, M., Yepes, G., Gottlöber, S., & Springel, V. 2006, MNRAS, 371, 401
Iliev, I. T., Mellema, G., Pen, U.-L., et al. 2006, MNRAS, 369, 1625
Iliev, I. T., Mellema, G., Shapiro, P. R., Pen, U.-L., Mao, Y., Koda, J., & Ahn, K. 2012, MNRAS, 423, 2222
Iliev, I. T., Mellema, G., Ahn, K., et al. 2014, MNRAS, 439, 725
Jenkins, A., Frenk, C. S., White, S. D. M., et al. 2001, MNRAS, 321, 372

Jensen, H., Datta, K. K., Mellema, G., et al. 2013, MNRAS, 435, 460
Kaiser, N. 1987, MNRAS, 227, 1
Kitayama, T., Tajiri, Y., Umemura, M., Susa, H., & Ikeuchi, S. 2000, MNRAS, 315, L1
Komatsu, E., Dunkley, J., Nolta, M. R., et al. 2009, ApJS, 180, 330
Komatsu, E., Smith, K. M., Dunkley, J., et al. 2011, ApJS, 192, 18
Lacey, C., & Cole, S. 1993, MNRAS, 262, 627
Lidz, A., Zahn, O., Furlanetto, S. R., et al. 2009, ApJ, 690, 252
Majumdar, S., Bharadwaj, S., & Choudhury, T. R. 2012, MNRAS, 426, 3178
Majumdar, S., Bharadwaj, S., & Choudhury, T. R. 2013, MNRAS, 434, 1978
Mao, Y., Shapiro, P. R., Mellema, G., et al. 2012, MNRAS, 422, 926
Maselli, A., Ferrara, A., & Ciardi, B. 2003, MNRAS, 345, 379
McQuinn, M., Zahn, O., Zaldarriaga, M., Hernquist, L., & Furlanetto, S. R. 2006, ApJ, 653, 815
McQuinn, M., Lidz, A., Zahn, O., et al. 2007, MNRAS, 377, 1043
Mellema, G., Iliev, I. T., Pen, U.-L., & Shapiro, P. R. 2006, MNRAS, 372, 679
Mellema, G., Iliev, I. T., Alvarez, M. A., & Shapiro, P. R. 2006, New Astronomy, 11, 374
Mellema, G., Koopmans, L. V. E., Abdalla, F. A., et al. 2013, Experimental Astronomy, 36, 235
Mesinger, A., & Furlanetto, S. 2007, ApJ, 669, 663
Mesinger, A., Furlanetto, S., & Cen, R. 2011, MNRAS, 411, 955
Mesinger, A., Ferrara, A., & Spiegel, D. S. 2013, MNRAS, 431, 621
Merz, H., Pen, U.-L., & Trac, H. 2005, New Astronomy, 10, 393
Mitra, S., Choudhury, T. R., & Ferrara, A. 2012, MNRAS, 419, 1480
Okamoto, T., Gao, L., & Theuns, T. 2008, MNRAS, 390, 920
Paciga, G., Albert, J. G., Bandura, K., et al. 2013, MNRAS, 433, 639
Page, L., Hinshaw, G., Komatsu, E., et al. 2007, ApJS, 170, 335
Parsons, A. R., Liu, A., Aguirre, J. E., et al. 2013, arXiv:1304.4991
Patil, A. H., Zaroubi, S., Chapman, E., et al. 2014, arXiv:1401.4172
Planck Collaboration, Ade, P. A. R., Aghanim, N., et al. 2013, arXiv:1303.5076
Razoumov, A. O., Norman, M. L., Abel, T., & Scott, D. 2002, ApJ, 572, 695
Rees, M. J. 1986, MNRAS, 218, 25P
Ricotti, M., Gnedin, N. Y., & Shull, J. M. 2002, ApJ, 575, 33
Santos, M. G., Ferramacho, L., Silva, M. B., Amblard, A., & Cooray, A. 2010, MNRAS, 406, 2421
Semelin, B., Combes, F., & Baek, S. 2007, AAP, 474, 365
Shapiro, P. R., Mao, Y., Iliev, I. T., et al. 2013, Physical Review Letters, 110, 151301
Sobacchi, E., & Mesinger, A. 2013, MNRAS, 432, 3340
Sobacchi, E., & Mesinger, A. 2014, MNRAS, 571
Sokasian, A., Abel, T., Hernquist, L., & Springel, V. 2003, MNRAS, 344, 607
Thomas, R. M., Zaroubi, S., Ciardi, B., et al. 2009, MNRAS, 393, 32
Thoul, A. A., & Weinberg, D. H. 1995, ApJ, 442, 480
Thoul, A. A., & Weinberg, D. H. 1996, ApJ, 465, 608
Tingay, S. J., Goeke, R., Bowman, J. D., et al. 2013, Pub. Astro. Soc. Australia, 30, 7
Trac, H., & Cen, R. 2007, ApJ, 671, 1
van Haarlem, M. P., Wise, M. W., Gunst, A. W., et al. 2013, AAP, 556, A2
White, R. L., Becker, R. H., Fan, X., & Strauss, M. A. 2003, AJ, 126, 1
Yatawatta, S., de Bruyn, A. G., Brentjens, M. A., et al. 2013, AAP, 550, A136
Zahn, O., Zaldarriaga, M., Hernquist, L., & McQuinn, M. 2005, ApJ, 630, 657
Zahn, O., Lidz, A., McQuinn, M., et al. 2007, ApJ, 654, 12
Zahn, O., Mesinger, A., McQuinn, M., et al. 2011, MNRAS, 414, 727
Zaroubi, S., de Bruyn, A. G., Harker, G., et al. 2012, MNRAS, 425, 2964